

Conceptual Design of a Manned Reconnaissance Airplane for Martian Atmospheric Flight

A project present to
The Faculty of the Department of Aerospace Engineering
San Jose State University

in partial fulfillment of the requirements for the degree
Master of Science in Aerospace Engineering

By

Jose L. Ferreira

May 23, 2018

approved by

Dr. Sean Montgomery
Faculty Advisor



Table of Contents

	1. Introduction	
.....	3
	2. Mission Profile	
.....	3
	3. Preliminary	
Configuration.....	4
	3.1 Overall	
Configuration.....	4
	3.1.1.1 Selection of Propulsion	
System.....	9
	3.1.1.2 Electric	
Propulsion.....	9
	3.1.1.3 Fuel Cell	
Propulsion.....	13
	3.1.1.4 Battery	
Propulsion.....	14
	3.1.1.5 Combustion	
Propulsion.....	14
	3.1.1.6 Internal Combustion	
Engines.....	15
	3.1.1.7 Piston	
Expander.....	16
	3.2 Selection of the Propulsion	
System.....	17
	3.2.1 Selection of the	
Propeller.....	19
	3.2.2 Selection of the Landing	
Gear.....	2

	4. Mission Weight	
Estimates.....24	
	5. Performance Constraint	
Analysis.....	29	
	5.1Stall	
Speed.....29	
	5.2Take-off	
Distance.....30	
	5.3Landing	
Distance.....31	
	5.4Speed	
Constraints.....32	
	5.5Drag Polar	
Estimation.....33	
	5.6Climb	
Constraints.....35	
	5.7Matching	
Plot.....36	
	6. Configuration of the Propulsion	
System.....37	
6.1Engine.....37	
6.2Propellers.....38	
	7. Fuselage	
Design.....39	
	8. Wing	
Sizing.....42	
	9. Design of the High-Life	
Devices.....54	
	10.Design of the Empennage and the Longitudinal and Directional controls.....59	
	11.Design of the Landing Gear and Weight and Balance.....61	

	11.1 Landing Gear	
Design.....61	
	11.2 Weight and	
Balance.....65	
	12.Stability and	
Control.....67	
	12.1 Static Longitudinal	
Stability.....67	
	12.2 Directional	
Stability.....70	
14.Conclusions.....		
	73
References.....		
	75
Appendix.....		
	76

1. Introduction

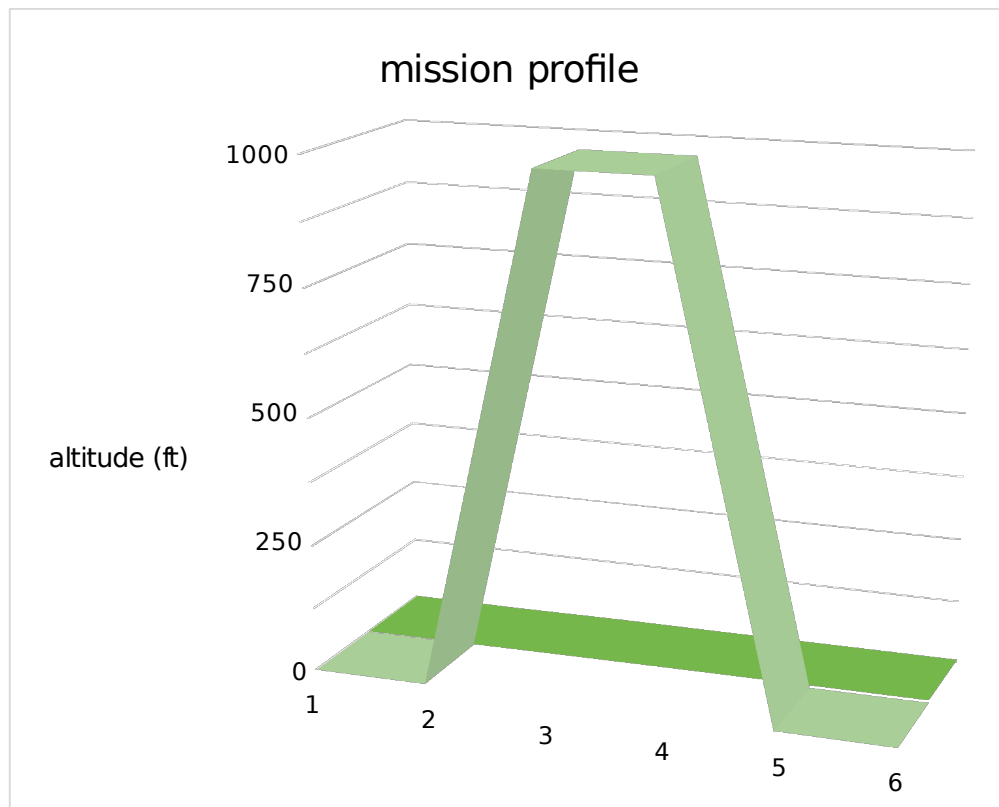
As humankind prepares to send the first ever manned missions to Mars, it has become essential to develop the tools that will make exploration of the Red Planet possible. For years, research on the feasibility of using aerial vehicles capable of flying in the Martian atmosphere have uniquely concentrated on the development of unmanned aircraft. There are several reasons why no serious proposals for the development of manned aircraft have been made. Flying in the Martian atmosphere is a challenging endeavor due to the physical characteristics of the atmosphere itself. In fact, the low Reynolds number, high Mach number conditions characteristic of the airless, CO₂-rich Martian atmosphere impose serious constraints to aircraft designers. Due to challenges associated with aerodynamic flight in the Red Planet, this report involves the conceptual design of a prospective airplane capable of flying in the Martian atmosphere under a set of given operational requirements.

2. Mission Profile

Because the purpose of this report concentrates on the determination of important design parameters and conditions required in the development of a two-seater aircraft capable of operating in the Martian atmosphere under a pre-determined flight envelope,

logistical requirements such as storage of the airplane and/or its components during a trip from the Earth to Mars, and other deliverance methods of such once in Mars, will be omitted.

The proposed vehicle must be capable of carrying up to two crewmen with a predetermined payload of 120 Lbs. (equivalent to a weight of 45 Lbs. on Mars), consisting of a low-altitude reconnaissance camera and survival equipment. The mission involves low-altitude flights at cruising altitudes of no more than 1,000 feet above the zero-elevation datum (6.105 mbar constant pressure reference \bar{c}^1 , and a range of 1,500 miles; while performing basic maneuvers like takeoff, climb, cruise, descend and the landing stages of the mission profile depicted below.



Graph 1. Mission profile of the Mars airplane

3. Preliminary Configuration

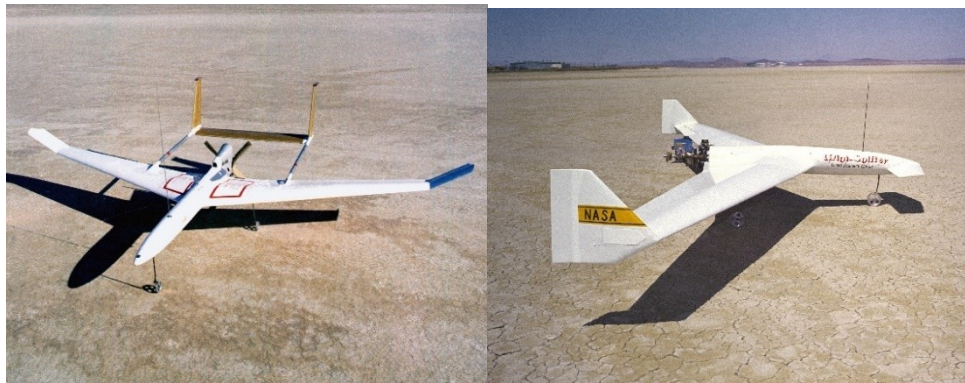
The preliminary configuration of the airplane is based primarily on the atmospheric characteristics of Mars. In summary, the thin atmosphere of the planet, including a density that is 6% that of Earth's at the zero-elevation datum, imposes great constraints or limitations to the performance and aerodynamic capabilities of any atmospheric flying

vessel. Lift generation, for instance, is greatly reduced even at the very low altitudes described in the mission profile. This limitation requires careful sizing and design of lifting surfaces capable of generating the lift necessary for flight. Furthermore, due to the low Reynolds number, low Mach number characteristics of the Martian atmosphere, selection of a proper propulsion system becomes critical.

3.1 Overall Configuration

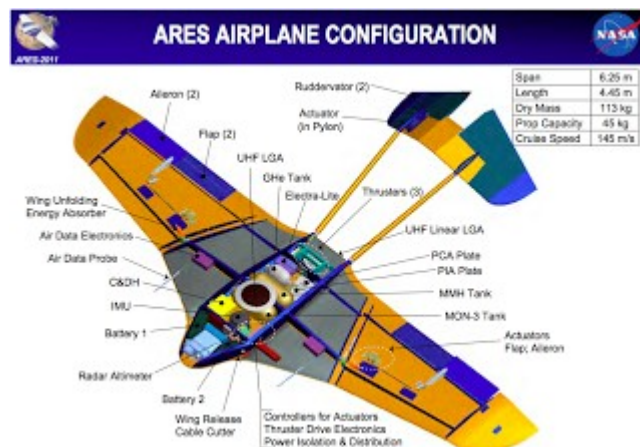
Due to the previous challenges, various unmanned Mars airplane concepts proposed have explored different configurations especially selected to maximize lift generation while minimizing weight and drag.

Although no originally envisioned to fly in Mars, NASA's *mini-sniffer* became an obvious candidate for eventual missions to Mars due to its performance at very low atmospheric density conditions. Different variants of this concept relied on both conventional and canard configurations, as shown in picture 1.



Picture 1. Mini-Sniffer configurations. [2]

Other visionary concepts that followed the *Mini-Sniffer* used similar configurations, including the Aerial Regional-scale Environmental Survey *ARES* aircraft (picture 2), which like the second version of the *Mini-Sniffer* (picture 1, left) relied on a conventional configuration with an inverted V-tail.

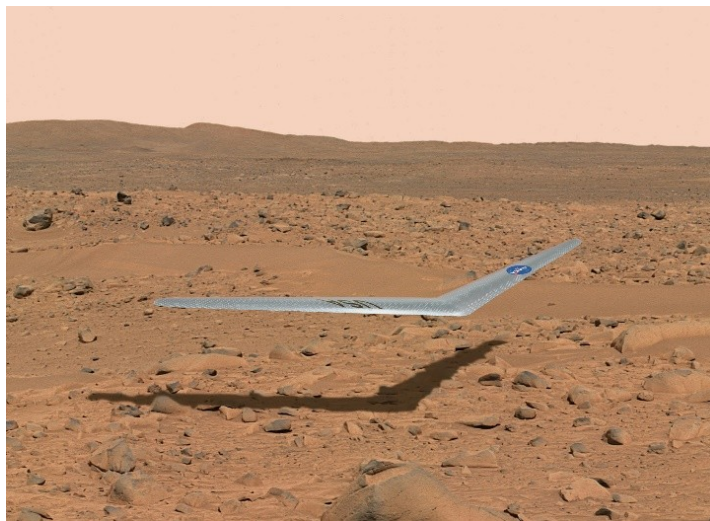


Picture 2. ARES configuration [3]

Others like NASA's *MATADOR* and *Prandtl-M* concepts (figures 3 and 4) take advantage of the tailless, flying wing configuration to eliminate the weight penalties associated with tail structures.



Picture 3. MATADOR Mars airplane. [4]



Picture 4. Prandtl-M concept. [5]

Other flying-wings that could potentially be retrofitted for missions in Mars include the unmanned, solar-powered *NASA Pathfinder*. A second, more efficient version of the original prototype, the *NASA Pathfinder Plus* features a larger wing surface area.



Picture 5. NASA Pathfinder (L) and NASA Pathfinder Plus (R). [6] [7]

Trade-Off Studies of Possible Configurations

The different pros and cons associated with the previous airplane configurations are now examined. The selected configuration for the proposed Mars airplane will depend on the especial performance and aerodynamic conditions that must be met in order to efficiently operate in Mars.

Conventional Configuration:

If it is desirable to naturally provide the airplane with an optimal level of stability and control in pitch and yaw without the need of complex mechanisms, the conventional, or aft-tail configuration is the most beneficial. In fact, tailless airplanes are inherently unstable, making them hard to control. In flying wings, for example, vital restoration of nose-down pitching moments can only be accomplished artificially with the addition of highly complex and costly automatic control methods. Favorable contributions of the empennage to the yaw and directional stability of an airplane through innate characteristics like the weathervane effect are reduced or absent in other configurations.

There are two major disadvantages associated with aft-tail designs. In contrast to tailless layouts like canards and flying wings, conventional layouts introduce weight and drag penalties associated with the empennage; this diminishes aerodynamic efficiency and performance.

Flying Wings:

Based on the previous assessment regarding conventional configurations, flying wings would be ideal for critical missions where weight and drag minimization are mandatory. In fact, tailless aircraft like the *Matador* and *Prandtl-M* have higher L/D ratios than other configurations.

There exist, however, significant drawbacks associated with flying wings. Inherently low CL_{max} generation, which requires high angles of attack during take-off and landing, and reduced wing loading (W/S), are important considerations to be kept in

mind in the design of a prospective Martian aerial vehicle. Indeed, due to limited CL_{max} , flying wings are generally inefficient during cruise flight and maneuvering.

Deflection of trailing edge flaps on tailless aircraft induces nose-down pitching moments and associated instability during the takeoff and landing stages of flight, where optimal control to achieve maximum lift, is required.

Furthermore, flying wings lack inherently good stability and control characteristics. In the absence of a tail, and therefore a moment arm, yaw control in flying wings must be obtained by alternate means due to the lack of weathercock stability. And although sweep, washout, tip-mounted fins or reflex airfoils can supplement the generation of pitch stability, which tailless flying wings must generate themselves, these tend to reduce lift, thus eliminating the high L/D advantage that flying wings possess.

Canards:

If a choice for a pusher arrangement of the Mars airplane is considered, adoption of a canard layout may be convenient. This canard-pusher arrangement can be seen in one of the two versions used by the *Mini-Sniffer*.

One possible advantage of a canard layout for flight in Mars is that if the foreplane is used as a lifting surface, it could enhance lift generation.

Drawbacks associated with the canard configurations include the possible degeneration of the wing lift distribution caused by the foreplane downwash. Undesirable stall behavior generally seen in canard layouts can prove critical in thin atmospheric conditions as those found on the Red Planet. It must be ensured, for instance that a canard is sufficiently loaded while approaching stall speeds so that the canard stalls before the wing; this condition makes canard sizing highly critical. The location of the fuel tanks is another important characteristic to keep in mind in the design process of canards. In this configuration, the center of gravity of the fuel tank is generally located farther aft of the airplane c.g.; it then should be desirable to find a suitable location for the fuel tanks so that a minimal c.g. travel occurs and longitudinal stability is avoided.

Another engineering concern related to the use of canards involves flap extension during critical phases of flight. For instance, the operation of large, powerful flaps during missions in the red planet would create large pitching moments that may be hard to balance by the foreplane.

Selection of the Overall Configuration

Based on the pros and cons that each of the previously analyzed configurations offer, and keeping in mind the maximum lift, minimum weight and drag constraints imposed by the existing conditions, it is appropriate to adopt the conventional configuration.

There are several reasons for this selection; first, airplanes with aft-tails are inherently stable, offering good controllability and stability during flight without resorting to feedback systems or other special design arrangements that may compromise required aerodynamic and performance capabilities of the airplane. This

benefit may be especially important in the near vacuum of the planet, where control surface response may not be optimal.

Although the addition of weight related to an empennage is contrary to the requirement of weight minimalization, it could be lessened by adopting a simple twin-boom tail, like that of the *ARES* or the second version of the *Mini-Sniffer*. Similarly, drag minimalization in the presence of a tail could be accomplished by minimizing surface area, and thus, skin friction.

Certainly, other important reasons for the adoption of a conventional configuration for missions in Mars are the result of the risks, costs and concerns associated with the tailless and canard configurations previously covered.

3.1.1 Selection of the Propulsion System

Due to the challenges associated with thrust generation in Mars, where typical, air-breathing engines could not operate, the selection of the propulsion system is, without a doubt, a highly critical aspect.

In addition to the importance of choosing an engine with low operational risks, and with the capacity to deliver the required power output, range and endurance dictated by the mission at hand, the weight of such powerplant is equally important.

For this purpose, electric, combustion and rocket propulsion systems now considered are categorized based on individual weight, range, endurance and risk of operation.

In order to quantify the behavior and performance of these three types of propulsion systems under similar flight conditions, a study on the development of possible powerplant(s) for the *ARES* concept⁸⁹ is now referenced. A trade-off

study involving weight, range, endurance and risk of operation for these propulsion systems is conducted at 1-hour, 2-hour and 4-hour flight durations using powerplants with an individual mass of 63 Kg. installed in common airframe.

At the conclusion of this section, a tabulated summary of the empirical data will be used to highlight the benefits and disadvantages associated with each individual propulsion system that could theoretically be adapted for Martian atmospheric flight.

3.1.1.1 Electric Propulsion

Because these systems require no propellant, some obvious advantages of using electric powerplants include the weight savings and lower risk of operation associated with chemical propulsion. In addition, electrical systems are highly efficient, with motor mass significantly lower than that of their jet, piston and rocket counterparts. However, power consumption, arcing and

cooling requirements are some of the challenges that must be carefully addressed if this type of propulsion is to be chosen to power a Mars airplane.

Power requirements

In order to quantify the power requirements for the prospective Mars airplane if electric propulsion is selected, a comparative analysis using existing data for three high-altitude aircraft is useful:

Airplane	Alt. _{cr} (kft)	V _{cr} (m/s)	P _{total} (hp) at alt	P _{total} (kW) at alt	P _{cr} (kW) 75%	T (kN)
Condor	67	103	362	270	202.5	1.97
Strato	78	140	800	597	447.75	3.2
Helios	87	10	47	35	26.25	2.63

Table 1. Power data for different high-altitude aircraft.

For electric propulsion systems, the power required can be calculated as:

$$P = \frac{TV}{\eta_t}$$

Where the thrust T is in Newtons, the flight velocity V is in m/s, and the total efficiency of the system η_t of the system is calculated as:

$$\eta_t = \eta_e \eta_m \eta_g \eta_p$$

η_e = efficiency of the control electronics

η_m = efficiency of the motor

η_g = efficiency of the gearbox

η_p = efficiency of the propeller

Assuming electric propulsion in steady, cruise flight conditions for the Boeing Condor at 75% power available using recorded data²⁶, a thrust level $T =$

1.97 kN, cruise velocity $V_{cr} = 103 \frac{m}{s}$, in addition to the following efficiencies

measured in the study by Colozza⁸,

$$\eta_e = 0.98$$

$$\eta_g = 0.85$$

$$\eta_p = 0.85$$

In addition, a measured motor efficiency for the EMRAX 268²⁵, a small but powerful electric motor for powering electric airplanes

$$\eta_m = 0.98$$

$$\eta_p = 0.98 * 0.98 * 0.85 * 0.85 = 0.694$$

$$P_{req} = \frac{TV_{cr}}{\eta_t} = \frac{1.97 \text{ kN} \times 103 \frac{\text{m}}{\text{s}}}{0.694} = 292 \text{ kW}$$

This indicates that under the assume efficiencies and similar flight conditions, electric powerplants require 30.5% more power than internal combustion engines.

$$P_{req} = TV_{cr} = 1.97 \text{ kN} \times 103 \frac{\text{m}}{\text{s}} = 202.9 \text{ kW} \quad (\text{Condor, cruise, piston engine})$$

Overall Powerplant Mass

Modern electric motors like the EMRAX 268 especially designed for electric aircraft offer excellent power-to-weight ratio P/W which makes them attractive for light airplanes.

By once again referencing high-altitude airplanes like the Boeing Condor and the Grob Strato (both piston, turbocharged powered airplanes), a comparative analysis between electric and internal combustion engines from a mass/weight standpoint can be conducted:

Airplane	Powerplant	P _{out} (kW)each	W _{dry} (kg)	P/W (kW/kg)
Condor	2xContinental TSOL-300-2 turbocharged piston	136	121.5*	0.89
Strato	2xTeledyne Continental TSIO-550 turbocharged piston	298	195.4	1.15

Table 2. Powerplants for the Condor and Strato.

Published data for the EMRAX 268 motor shows a power-to-weight ratio,

$$\frac{P}{W} = 11.6 \frac{kW}{kg}$$

superior than those for the Condor and Strato engines. However, this advantage would be reduced significantly once the EMRAX 268 is scale up to an appropriate size, in order to guarantee that there are not excessive bending loads associated with the operation of large propellers with small motors (*The EMRAX 268 is 3.6 inches long and 10.6 inches in diameter, picture 6*).



Picture 6. EMRAX 268 electric motor ²⁵

Assuming a possible $P/W = 2 \text{ kW/kg}$ for a required larger version of this motor, and assuming the previously calculated power required for cruise flight for the

Condor, $P_{req} = 202.9 \text{ kW}$, obtain

$$W_{motor} = 51 \text{ kg (per engine)}$$

which is approximately 58% less weight than that of the Condor's Continental TSOL-300-2 piston engine (121.5 kg).

Electric arcing

Due to the rarified, thin atmosphere of Mars composed mostly of CO₂, arcing from electrical motors can be a major concern. If an electric propulsion system is necessary, it may be appropriate to select a brushless DC motor, which although less efficient at higher power settings than brushed DC motors, are less prone to arcing.

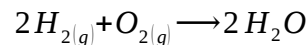
Cooling Requirements

Depending on their particular thermal mass, an electric powerplant may require a significant amount of convective cooling to prevent motor overheating. The lack of sufficient natural cooling in the thin Martian atmosphere is therefore a major disadvantage, and possible artificial solutions may impose other challenges.

For instance, structural or mechanical devices connected to the motor that could facilitate heat transfer to the airflow impose drag and weight penalties. Similarly, the possible addition of a liquid cooling system could add significant weight to the system.

3.1.1.2 Fuel Cell Propulsion

This practical concept uses fuel cells to convert hydrogen and oxygen into electrical energy and water. In the direct combination reaction when hydrogen and oxygen react to form water:



8 grams of oxygen are consumed for every gram of hydrogen.

A summary of experimental data⁸ using a fuel cell propulsion system with individual mass of 63Kg. and a continuous power output of 7,147 W, shows the following performance of fuel cells for 1h, 2h, and 4h mission durations:

	1h	2h	4h
H ₂ mass	0.484 ka	0.968 ka	1.936 ka
O ₂ mass	3.872 ka	7.744 ka	15.49 ka
H ₂ volume	0.024 m ³	0.053 m ³	0.11 m ³
O ₂ volume	0.01 m ³	0.021 m ³	0.041 m ³

Table 3. Mass and volume requirements at different endurance

clearly, a critical factor in the design of a fuel cell propulsion system involves mass and volumetric oxygen requirements, especially as endurance is increased.

Energy density could also be estimated experimentally by Colozza based on a thrust level of 35 N for the fuel cell system describe above.

Empirical data for the 1h, 2h and 4h missions is shown below:

	1h	2h	4h
Total System Mass (kg)	47.93	54.25	66.97
Specific Energy (W-h/kg)	239	395	584

Table 4. Total mass and specific energy for fuel cell.

this table shows that as the time of operation is doubled, the specific energy of the system is steadily increased. This is due to the fact that as the time duration is increased, only the reactant masses and their respective storage tanks must increase in volume and mass, while those of other system components remain unchanged. This makes fuel cell propulsion systems attractive for missions in Mars.

3.1.1.3 Battery Propulsion

Although weight savings associated with the use of electric motors can be significant, as previously demonstrated, electric propulsion systems still don't adapt well to missions with extended range and endurance.

Today, no battery with the capacity to fulfill the special requirements for manned missions in Mars is available.

Available Lithium-ion batteries (Li-ion) suitable for automotive and aviation purposes offer an average specific energy of 0.36 – 0.875 MJ/kg compared to 46.4MJ/kg and 42.8MJ/kg for gasoline and kerosene, respectively.

Furthermore, the energy density of Lithium polymer batteries is substantially lower than those of gasoline and kerosene. These properties are summarized below:

Storage Material	Specific Energy (MJ/kg)	Energy Density (MJ/L)
Gasoline	46.4	34.2
Kerosene	42.8	37.4
Li-ion Battery	0.36-0.875	0.9-2.63

Table 5. Specific energy and energy density for different systems

These properties clearly demonstrate the mass and volumetric constraints that are associated with readily available batteries.

One such example, the Solar Impulse, uses four 21 kWh lithium-ion batteries, each connected to an electric motor with an individual power output of 7.5 kW (10 hp).

Each one of these batteries weighs 633 kg with reported energy densities of 243 Wh/kg (Solar Impulse I) and 260 Wh/kg (Solar Impulse II).

Because the batteries of this airplane weigh roughly a quarter of the airplane's overall weight, airplane weight and payload reduction are critical.

However, the most critical design constraint of the Solar Impulse is the capacity of the Li-ion batteries to store the required charge for the motors to produce 6 kW of continuous power.

Unlike chemical powerplants which burn their propellant as operation time progresses, the mass of battery-based propulsion systems remains virtually unchanged. This disadvantage would be especially detrimental for missions in Mars, where the thin atmosphere could create challenges for heavier airplanes while on the final approach and landing stages of flight.

3.1.1.4 Combustion Propulsion

Because the planet's atmosphere is composed mainly on CO₂ (95.97%) and just 0.146% oxygen, special considerations must be given to the adaptation of existing airbreathing propulsion systems. However, if the capabilities that combustion engines can offer are essential to achieve the required performance as specified in the mission profile, then proper modifications to existing airbreathing powerplants must be made.

3.1.1.5 Internal Combustion Engines

Probable fuels

The selection of an optimal fuel that can deliver the energy required by the engine is a critical aspect in the modification/design of a prospective powerplant.

There are, in addition, significant logistical concerns associated with the selection of propellant. Because of the long transit times to Mars which make constant supply of fuel difficult, fuel storage with minimal degradation must be addressed.

Similarly, due to the extreme cold temperatures during both ground and flight operation (in-situ temperature values recorded by the Viking I and II spacecraft range between 1F° (-17.2 C°) and -161F° (-107 C°)) it must be ensured, in the absence of a heating system, that the fuel has a freezing point low enough so that it remains liquid. A tabulated summary of possible fuels is summarized next:

Fuel	Boil. Point (C°)	Freez. Point (C°)	React	Toxic	Phase*
H ₂	-253	-259	yes	no	gas
NH ₃	-33.4	-77.7	yes	yes**	gas
N ₂ H ₄	113.4	1.5	yes	yes	solid
MMH	89.2	-52.5	yes	yes	liquid
UDMH	53.8	-57.2	yes	yes	liquid
RP-1	185	-40	yes	yes	sol/liq
CH ₄	-161	-183.9	no	no	gas
C ₂ H ₆	-42.2	-187.1	no	no	gas

Table 6. Properties of different fuels

*at mission temperatures

**at high concentrations

Probable oxidizers

The adaptation or conversion of available internal combustion engines for missions in the Martian atmosphere includes the requirement of an oxidizing agent; this, in turn, imposes additional weight penalties to the system.

The following table addresses the adaptation of several oxidizers based on the previously described temperature conditions on the surface of the planet.

Oxidizer	Boil. Point (C°)	Freez. Point (C°)	React	Toxic	phase*
O ₂	-183	-218.8	yes	no	gas
F ₂	-188.1	-219.6	yes	yes	gas
N ₂ O ₄ **	-9	-54	no	yes	liquid
ClF ₃	11.8	-76.6	yes	yes	liquid
IRFNA	~60	~-62.2	yes	yes	liquid
OF ₂	-145	-223.5	yes	yes	gas

Table 6. Properties of different oxidizers

*at mission temperatures

**NO 25% mixed

3.1.1.6 Piston Expander

This external combustion propulsion application involves the decomposition of fuel through catalytic reaction.

Although these engines have long been proven reliable in torpedo propulsion, their application to aircraft propulsion is still in experimental stages. Nevertheless, studies show that their application to high-altitude propulsion is promising, since it doesn't require air to operate and can burn virtually any mono/bi-propellant.

A piston expander version used in torpedoes is propelled by hydroxyl ammonium nitrate and diesel oil delivers high power density at low weight, including 0.9 to 1.2 kg/kW.

Because its SFC is quite high (2.7-4 kg/kW-h), it is more suitable, at the present state of technology, for short excursions at high altitudes. In the 1970s, NASA's mini-sniffer used a piston-expander Akkerman engine especially designed to power the airplane at altitudes of up to 100,000 ft.

This engine was designed to produce 22 kW (30 hp) using hydrazine monopropellant, with an SFC of 2.7 kg/kW-h. A modified version of this airplane for special use in the Martian atmosphere was proposed, including a smaller Akkerman engine with the following reported characteristics:

P(kW)	Fuel	Oxidizer	Weight (kg)	P/W (kW/kg)	SFC (kg/kW-h)
11	hydrazine	n/a	6.8	1.62	2.7*

Table 7. Data for the Akkerman engine

*data taken from original version

Experimental results obtained by Colozza et al show the mass and volume requirements for a piston expander engine based on a power requirement of

7142 W for 1h, 2h and 4h time durations. In this analysis, three different mono/bipropellant combinations known to remain liquid during mission temperatures are chosen:

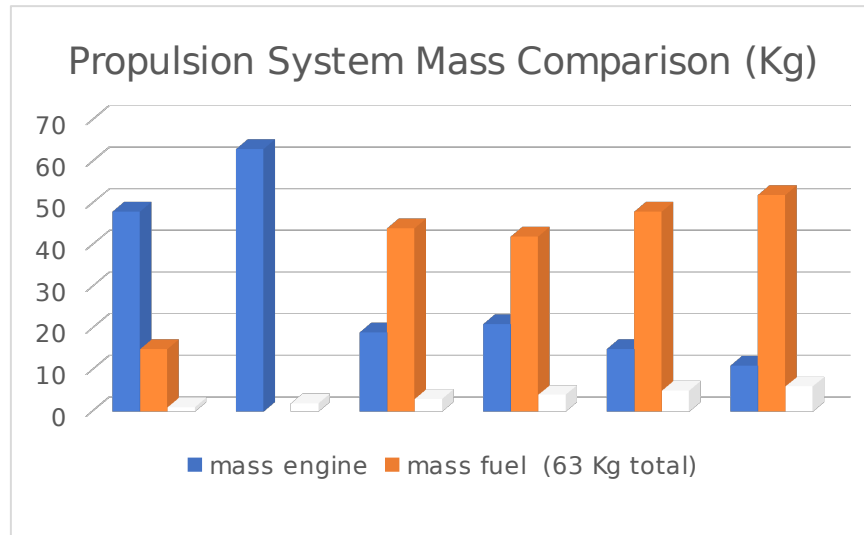
time duration	1 h		2 h		4 h	
fuel/oxid	vol (m ³)	mass (kg)	vol (m ³)	mass (kg)	vol (m ³)	mass (kg)
N ₂ H ₄	0.014	14.43	0.0286	28.86	0.0573	57.71
MMH/N ₂ O ₄	0.0113/0.012	9.86/17.26	0.023/0.0238	19.72/34.51	0.0451/0.0476	39.45/69.04
UMDH/N ₂ O ₄	0.0089/0.011	7.02/15.79	0.0177/0.0218	14.03/31.56	0.0354/0.0436	28.08/63.17

Table 8. mass and volumetric requirements at different endurances.

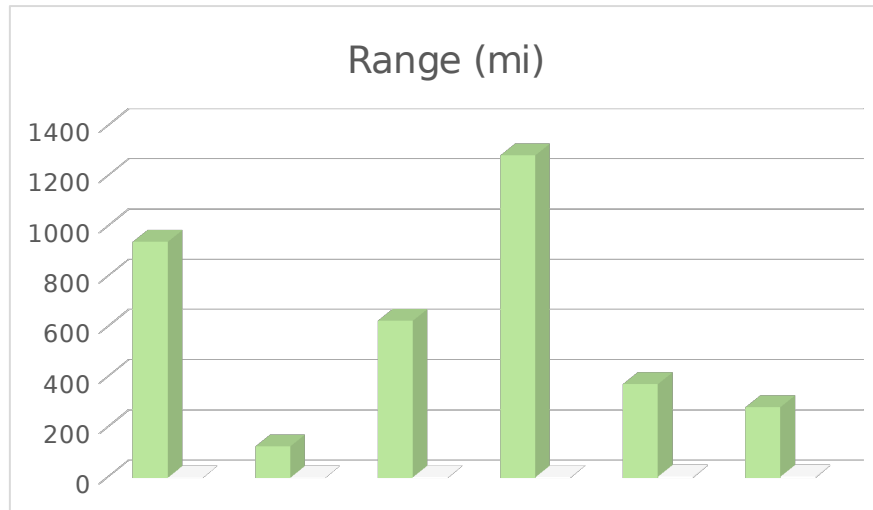
Propellant mass and volume requirements for the hydrazine monopropellant and the hydrazine, nitrogen tetra-oxide bipropellant combinations are proportional to mission time duration.

3.2 Selection of the Propulsion System

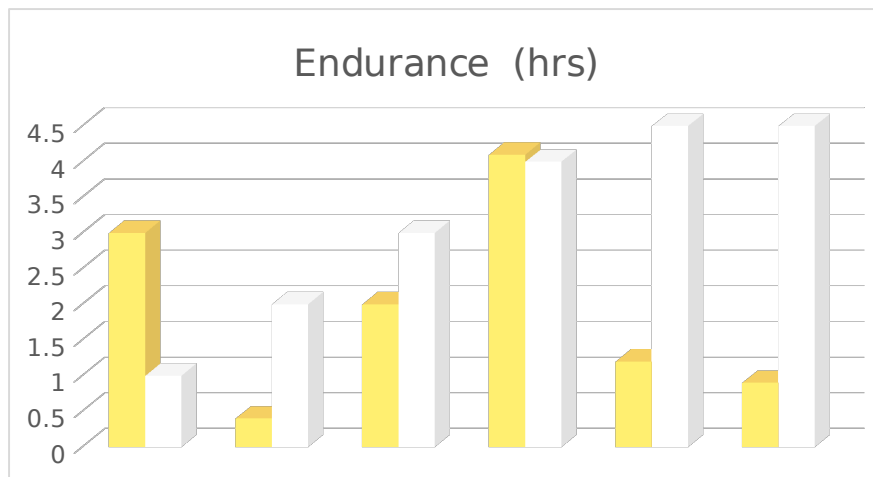
The following empirical data summarizes the performance of each of the considered propulsion systems based on range, endurance and the highly critical powerplant mass. Data collected at the 1, 2 and 4-hour flight durations show that 4-cycle engines could adapt better to the characteristics of the proposed airplane.



Graph 2. Engine and fuel mass comparison for the ARES mission



Graph 3. Propulsion system vs. range for the ARES.



Graph 4. Propulsion system vs. endurance of the ARES

According to projections of these charts and based on weight constraints and range and endurance requirements, the most advantageous propulsion systems for reconnaissance missions on Mars include the fuel cell, electric engine, and the modified 4-cycle internal combustion engine.

Based on performance, battery-based engines are the least desirable. Their range capability, for instance, is the lowest of all, with an approximate maximum range of just 126 miles under tested conditions. An important advantage of battery-based propulsion system involves the lower operational risks due to its simplicity in operation and design, including fewer mechanical parts than the other systems.

Rocket systems, on the other hand, are perhaps the obvious choice if superior operational performance during short range and endurance missions is desired. Another advantage of rocket systems over the fuel cell and internal combustion

engines involves the considerable less design challenges and operational risks associated with rocket engines.

These challenges and risks can become crucial if special propeller design and operational constraints required in Mars-bound fuel cell and internal combustion powerplants are considered. For example, the requirement to use larger, heavier propeller(s), capable of producing the superior efficiency required in low Reynolds number, high subsonic Mach number conditions would be a concern if fuel cell or 4-cycle internal combustion systems were preferred.

As the collected data suggests, if range and endurance are critical, then a 4-cycle internal combustion engine is the clear choice. Based on the experimental results and under the given conditions, 4-cycle internal combustion engines offer as much as four times the range and endurance than mono and bi-propellant rocket engines and roughly twice the range and endurance than piston expanders. It must be stressed, however, that this engine must be a modification of typical air-breathing 4-cycle internal combustion engines, and that special propellers must be designed in order to obtain the required efficiency at the given atmospheric conditions. It has been estimated, for instance, that the power transferred from a propeller to the airstream at altitudes of about 80,000 ft. on

Earth is about 30 times less than that at sea level ¹⁰.

3.2.1 Selection of the Propeller

Propeller design is a complex field in which multiple physical and geometrical variables must be carefully synchronized in order to efficiently transfer the power produced by the engine to the airflow; that is, thrust production.

Design of propellers that can be specifically adapted to low Reynolds number, high Mach number regimes, however, is a more arduous task involving more complex engineering challenges.

Although no particular studies for a unique "Martian propeller" has been proposed, few projects involving high altitude propeller-driven flight have been conducted.

On Earth, only a handful of propeller-driven airplanes, manned and unmanned, have been test flown in conditions that approximate those expected at Mars.

Boeing Condor:

In 1989, the Boeing Condor set the world altitude record for a propeller-driven aircraft, reaching an altitude of 67,028 ft. A remotely piloted reconnaissance airplane, the Condor used two 16 ft., 3-bladed variable pitch propellers especially designed by the Hartzell Propeller Company to efficiently operate through a very wide range of atmospheric densities.



Picture 7. Condor Unmanned Aerial Vehicle ^{20,21}

Perseus B:

Initially designed to reach altitudes of up to 80,000 ft. using a 14.4 ft. diameter propeller, the Perseus B reached a maximum altitude of 50,000 ft. using a special 9.2 ft. diameter pusher propeller. The larger, 22 Lb. (including pitch control mechanism) composite propeller was designed to absorb 67 hp of power at altitude.



Picture 8. Perseus B Remotely Piloted Aircraft ²²



NASA Dryden Flight Research Center Photo Collection
<http://www.dfrc.nasa.gov/gallery/photo/index.html>
NASA Photo: EC99-45152-6 Date: September 1999 Photo by: Tom Tschida

Perseus B Parked on Ramp - Close-up of Controllable-Pitch Pusher Propeller

Picture 9. Perseus B Medium Altitude Propeller . 23

In 1995, the Grob Strato 2C, using two 5-bladed propellers set the high-altitude world record (60,897 ft.) for a manned, piston-driven airplane. These variable pitch propellers, with a diameter of 19.7 ft. were designed to absorb 400 hp from the engine.



Picture 10. Grob Strato 2C MT 6m Propellers ²⁴

Design Approach:

Because a propeller's capacity to transfer the engine shaft power to the airstream is directly proportional to air density, the effective thrust generated by the propeller diminishes with altitude. The effects of this thrust deterioration are especially detrimental at very high altitudes; at 80,000 ft., for instance, the power absorbed by the propeller and transferred to the airstream is 1/30th that at sea level.

The important relationship between the thrust generated and air density is evident in the following equation:

$$T = c_t \rho n^2 d^4$$

Where,

c_t = coefficient of thrust

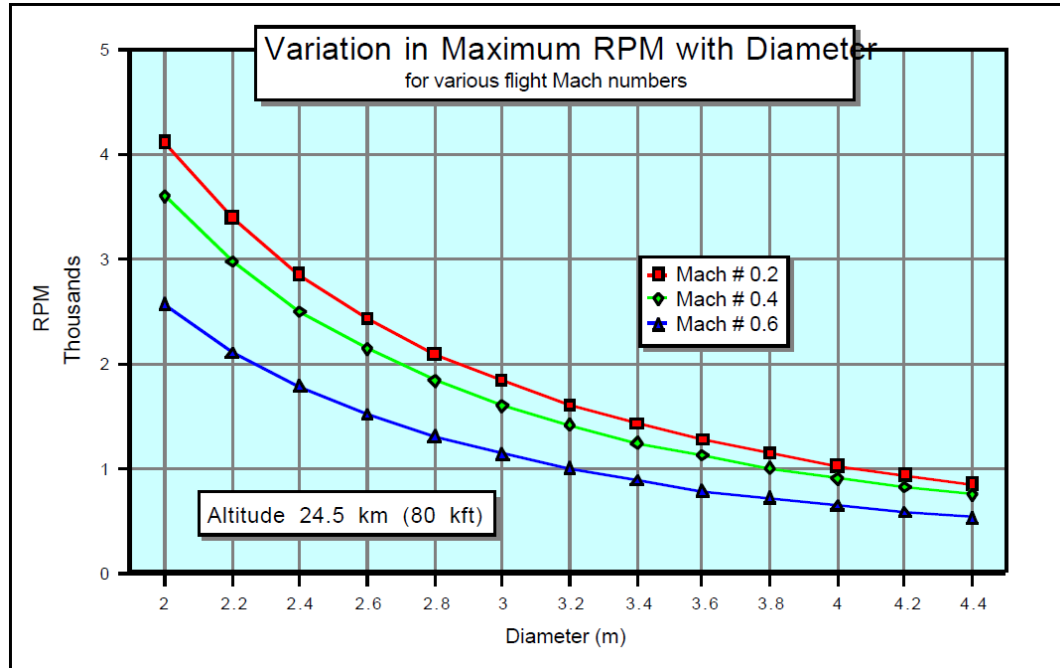
ρ = air density

n = propeller revolutions

d = propeller diameter

Aside from geometrical parameters of a propeller such as airfoil and twist, two important aspects that influence the performance of a propeller are RPM and diameter.

The operational RPM limit of a propeller at any altitude, for example, is restricted by Mach number at the propeller's tip. Ordinarily, manufacturers place this limit at 0.75; this is to ensure that no effects associated with the onset of supersonic flow at the tip adversely affect the performance of the propeller, or even destroy it.



Graph 5. Variation in Maximum RPM with Diameter for various flight Mach numbers. Data for an altitude of 80,000 ft ⁸.

As the graph indicates, increasing the diameter of the propeller decreases the required propeller RPM, which in turn decreases airstream velocity along the span of the propeller blade.

3.2.2 Selection of the Landing Gear

The requirement to operate large propellers imposes clearance restrictions between the propeller and the ground, imposing constraints for the design and disposition of the landing gear.

Based on available landing gear arrangements, the bicycle and tricycle configurations are arguably the most convenient for potential operations in the Red Planet due to their improved propeller ground clearance. The dusty, rocky soil constitution of the Martian soil may create structural and/or catastrophic damage to propeller blades if no proper precaution is taken in the design of the landing gear.

Due to the drag and weight constraints previously mentioned, it becomes necessary to produce a landing gear that is retractable yet light.

4. Mission Weight Estimates

Estimation of the take-off gross weight W_i , the empty weight W_E and the mission fuel weight W_F included in this section is conducted using the methodology recommended by Roskam¹¹.

In addition, the calculation of these weights is obtained using documented statistical and empirical data corresponding to propeller-driven aircraft under Earth conditions.

Educated guess of take-off weight:

Estimation of the take-off weight, based on extrapolation of existing data corresponding to aircraft with similar mission profiles or operational characteristics is a challenge, since no manned concepts have been proposed, and very limited data for unmanned Mars airplanes exists or is available.

For the sake of estimation, take-off weight will be approximated by referencing existing propeller-driven airplanes which designs depended primarily on weight and drag minimalization.

With an estimated $L/D = 25$, the *Rutan Voyager* set the flight endurance record in 1986 using a 939 Lb. airframe made of fiberglass, Kevlar and carbon fiber¹². Despite having an empty weight of 2,250 Lb. (1,020.6 Kg.), it weighted 9,694.5 Lbs. at take-off due to the large amount of fuel needed to complete its long-endurance mission. Although the *Voyager* had a different mission profile than that described in this report, it can nonetheless serve as a basis for the present weight estimation. Pertinent data for other high-altitude airplanes is summarized below.

airplane	crew	powerplant	max alt. (ft.)	WE (Lbs)	WTO (Lbs)	L/D
Boeing Condor	unmanned	2 x turbocharged piston (175 HP each)	67,028	8,000	20,000	40
Grob Strato	4	2 x turbocharged piston (402 HP each)	60,897	14,660	29,432	unk.
NASA Pathfinder	unmanned	6 x electric (2HP each)	71,530	N/A	560	18
Pathfinder Plus	unmanned	8 x electric (2HP each)	80,201	N/A	700	21

Table 9. Operational characteristics of different high-altitude airplanes

Assuming an airframe 15% heavier than the *Voyager's* in order to compensate for a prospective larger wing surface area,

$$W_{struct} = 939 \text{ Lbs.} + (939 \times 0.1) = 1,032 \text{ Lbs.} \quad *weight \text{ as measured on Earth}$$

Preliminary estimation for powerplant weight assumes two engines with a power output of 175 HP (each), similar to those used by the Condor¹³.

$$W_{eng} = 268 \text{ Lbs each (dry)}$$

in addition, two three-bladed composite propellers with an assumed individual weight of 100 Lbs.,

$$W_{pwr} = W_{eng} + W_{\dot{i}} = 536 \text{ Lbs.} + 200 \text{ Lbs.} = 736 \text{ Lbs.}$$

According to Torenbeek¹⁴ (Appendix A), data for short-haul piston airplanes shows typical weight fractions of 16% MTOW for fixed equipment and 30% for airframes.

Based on the assumed $W_{struct} = 1,080 \text{ Lbs.}$ calculated above, it is reasonable to assume $W_{feq} = 576 \text{ Lbs.}$

$$W_E = W_{struct} + W_{pwr} + W_{feq}$$

$$W_E = 1,032 + 736 + 576 = 2,345 \text{ Lbs.}$$

Analysis of the empty and take-off weights indicates ratios $\frac{W_{\dot{i}}}{W_E}$ of 2 and 2.5 for the

Strato and Condor, respectively. These airplanes, however, were designed for long endurance missions (the Condor carried large amounts of fuel for long endurance missions of up to 80 hours)

$$\text{assuming } \frac{W_{\dot{i}}}{W_E} = 1.5,$$

$$W_{\dot{i}_{guess}} = 1.5 \times W_E = 3,518 \text{ Lbs}$$

Calculation of maximum take-off weight based on fuel fractions:

Propeller efficiency:

The efficiency of a propeller is affected by both the propeller's diameter as well as number of blades. For instance, increasing diameter increases the propeller's efficiency, while adding more blades decreases it. However, adding more blades also increases thrust, which is one of the critical factors to keep in mind for the design of the Mars airplane. Based on these characteristics and on the analysis provided in section 3.1.3, a

2.8 m (110 in) diameter, three-bladed propeller with efficiency of 0.83 seems reasonable

10

Specific fuel consumption:

Due to its adaptivity to the atmospheric characteristics of Mars, it was previously decided to use a piston expander engine propelled by the UDMH, N₂O₄ combination.

Because data for the specific fuel consumption of this systems is not available,

$c_p = 0.8 \frac{lbs}{HP-hr}$ will be assumed for calculation purposes. This agrees with

statistical data for piston twin engine airplanes.

Lift to drag ratio: (at cruise)

The aerodynamic forces L and D are directly proportional to the density of the fluid flowing around the airfoil. Due to Mars low atmospheric density (100 times lower than Earth's at the reference altitude), obtaining a convenient lift-to-drag ratio, even at the low cruising altitude described in the mission profile becomes critical. High-performance,

high-aspect ratio aircraft like the *Lockheed Martin U-2*, can generate a $L/D = 25.6^{16}$,

while slower, high-altitude flying wings like the *Pathfinder-Plus* have a reported glide ratio of 21:1 (power off) ¹⁷. Based on the expectation that a high aspect ratio wing will

be required to fulfill the mission at hand, a lift-to-drag ration $L/D = 40$ will therefore be assumed in the preliminary calculations. This value agrees with a reported $L/D = 40$ for the Boeing Condor during cruise conditions.

Payload weight:

Taking as reference the standard weight for military crews of 200 Lbs. per person (including extra gear carried), a weight of 400 Lbs. corresponding to two crewmen will be assumed. In addition, a 120 Lb. payload consisting of a high-resolution camera and survival equipment is considered.

Therefore, a payload weight of 520 Lbs. will be used in the calculations.

$$W_{payload} = 520 \text{ Lbs. (*weight as measured on Earth)}$$

$$M_{f.c.} = 0.005$$

$$\eta_p (cr) = 0.83$$

$$c_p (cr) = 0.8 \frac{lbs}{HP-hr}$$

$$L/D \text{ (cr)} = 40$$

$$R = 1,500 \text{ s.m.}$$

Estimation of the take-off gross weight W_i

$$W_i = W_{OE} + W_F + W_{PL}$$

W_{OE} , the operating weight empty, is calculated as:

$$W_{OE} = W_E + W_{tfo} + W_{crew}$$

where the weight of trapped fuel and oil W_{tfo} can be approximated as 0.5% the take-off weight,

$$W_{tfo} = 0.005 W_i$$

Estimation of the mission fuel weight W_F

$$W_F = W_{F_{used}} + W_{F_{res}}$$

Where,

$$W_{F_{used}} = (1 - M_{ff}) W_i \quad \text{and} \quad M_{ff} = \frac{W_1}{W_i} \pi \frac{W_{i+1}^{i=7}}{W_i^{i=1}}$$

$$W_{F_{res}} = 0.25 W_{F_{used}}$$

M_{ff} calculation based on typical fuel weight fractions for twin-engine aircraft ¹¹

I) *Engine start and warm-up*

$$\left(\frac{W_1}{W_i} \right) = 0.992$$

II) *Taxi*

$$(W_2 / W_1) = 0.996$$

III) *Takeoff*

$$(W_3 / W_2) = 0.996$$

IV) *Climb*

$$(W_4 / W_3) = 0.990$$

V) *Cruise*

$$(W_5 / W_4) R_{cr} = 375 \left(\frac{\eta_p}{c_p} \right)_{cr} \left(\frac{L}{D} \right)_{cr} \ln \left(\frac{W_4}{W_5} \right) \text{ (*for propeller-driven aircraft)}$$

$$1,500 = 375 \left(\frac{0.83}{0.8} \right) (40) \ln \left(\frac{W_4}{W_5} \right)$$

$$\frac{W_5}{W_4} = 0.908$$

VI) *Descend*

$$(W_6 / W_5) = 0.992$$

VII) *Landing, taxi*

$$(W_7 / W_6) = 0.992$$

$$M_{ff} = \dot{i} \frac{W_1}{W_{\dot{i}}} \times \frac{W_2}{W_1} \times \frac{W_3}{W_2} \times \frac{W_4}{W_3} \times \frac{W_5}{W_4} \times \frac{W_6}{W_5} \times \frac{W_7}{W_6}$$

$$= 0.992 \times 0.996 \times 0.996 \times 0.990 \times 0.908 \times 0.992 \times 0.992 = 0.8706$$

Estimation of the empty weight W_E

$$W_E = inv. \log_{10} \left[\frac{\log_{10} W_{\dot{i}} - A}{B} \right]$$

Where the values for the regression coefficients A and B correspond to those of twin engine, propeller-driven composite aircraft ¹⁰

$$A=1130, B=1.0403$$

The tentative empty weight $W_{E_{tent}}$ is calculated as:

$$W_{E_{tent}} = W_{OE_{tent}} - W_{tfo} - W_{crew}$$

where $W_{OE_{tent}} = W_{\dot{i}_{guess}} - W_F - W_{PL}$

W _{TO} (Lbs)	W _{Fused} (Lbs)	W _F (Lbs)	W _{OE_{tent}} (Lbs)	W _{E_{tent}} (Lbs)	W _E (Lbs)	%W _E - W _{E_{tent}}
3300	426.95	533.69	2246.31	1829.81	1877.5 4	2.57
3325	430.18	537.73	2267.27	1850.64	1891.2 1	2.17
3350	433.42	541.77	2288.23	1871.48	1904.8 7	1.77
3375	436.65	545.82	2309.18	1892.31	1918.5 4	1.38
3400	439.89	549.86	2330.14	1913.14	1932.2 0	0.99
3425	443.12	553.90	2351.10	1933.97	1945.8 5	0.61
3450	446.36	557.95	2372.05	1954.80	1959.5 0	0.24
3475	449.59	561.99	2393.01	1975.64	1973.1 5	-0.13
3500	452.83	566.03	2413.97	1996.47	1986.7 9	-0.49
3525	456.06	570.08	2434.92	2017.30	2000.4 3	-0.84

3550	459.30	574.12	2455.88	2038.13	2014.0 7	-1.19
3575	462.53	578.16	2476.84	2058.96	2027.7 0	-1.53
3600	465.76	582.21	2497.79	2079.79	2041.3 3	-1.87

Table 10. Determination of weights

The take-off weight of the airplane can be obtained once the empty weight of the aircraft and its tentative value are within 0.5%,

$$W_i = 3,450 \text{ Lbs. (weight as measured on Earth)}$$

this weight is within 2% of the gross take-off weight previously estimated,

$$W_{i_{guess}} = 3,518 \text{ Lbs.}$$

5. Performance Constraint Analysis

The sizing of the aircraft will depend on the following stall, take-off distance, landing distance, cruise velocity and climb requirements.

5.1 Stall Speed

$$\rho_{(0 \text{ ft})} = 0.002377 \frac{\text{Kg}}{\text{m}^3} = 3.88064 \times 10^{-5} \frac{\text{slugs}}{\text{ft}^3}$$

$$C_{L_{max}} = 1.4$$

$$C_{L_{max_t}} = 1.8$$

$$V_{s_0} \leq 95 \text{ Kts} \approx 160 \frac{\text{ft}}{\text{s}} \quad (\text{engine idle, flaps extended})$$

$$V_{s_1} \leq 110 \text{ Kts} \approx 186 \frac{\text{ft}}{\text{s}} \quad (\text{engine idle, flaps retracted})$$

Stall requirements must be met at take-off gross weight W_i

Wing loading:

$$\frac{W}{S} < \rho_{\infty} V_s^2 \frac{C_{L_{max}}}{2}$$

Clean configuration

$$\frac{W}{S} < 3.88064 \times 10^{-5} \frac{\text{slugs}}{\text{ft}^3} * 186^2 \frac{\frac{\text{ft}}{\text{s}} * 1.4}{2}$$

$$\frac{W}{S} < 0.94 \frac{\text{Lb}}{\text{ft}^2}$$

Landing configuration:

$$\frac{W}{S} < 3.88064 \times 10^{-5} \frac{\text{slugs}}{\text{ft}^3} * 160^2 \frac{\frac{\text{ft}}{\text{s}} * 1.8}{2}$$

$$\frac{W}{S} < 0.9 \frac{\text{Lb}}{\text{ft}^2}$$

Therefore, to fulfill both requirements, $\frac{W}{S} < 0.9 \frac{\text{Lb}}{\text{ft}^2}$

5.2 Take-off Distance

Requirements

$$S_{TOG} = 1,700 \text{ ft.}$$

$$S_i = 1.66 S_{TOG} = 1.66 * 1,700 = 2,822 \text{ ft.}$$

where S_i and S_{TOG} are defined in table 6, appendix A

The following equation relates the take-off ground run (S_{TOG}) to the maximum take-off lift coefficient ($C_{L_{max_i}}$) and the take-off power loading of the airplane ($\frac{W}{P}$).

$$TOP_{23} = \frac{\frac{W}{S} \frac{W}{P}}{\sigma CL_{max}}$$

the density ratio σ is calculated as:

$$\sigma = \frac{\rho(95,144 \text{ ft})}{\rho(\text{msl})} = 0.01724$$

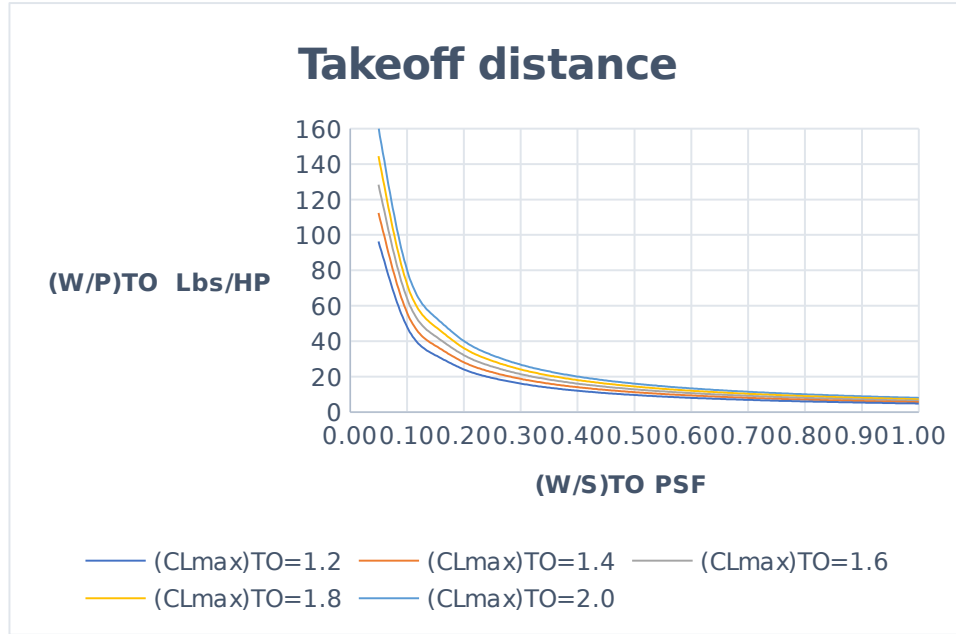
TOP_{23} , the take-off parameter for FAR23 propeller-driven airplanes, can be calculated from the following relation using the quadratic formula as:

$$S_{TOG} = 4.9 TOP_{23} + 0.009 TOP_{23}^2$$

$$TOP_{23} = \frac{-4.9 \pm \sqrt{4.9^2 - 4 * 0.009 * (-1700)}}{2 * 0.009} = 240.76 \wedge -785$$

$$TOP_{23} = \dot{i} \quad \underline{240.76}$$

This leads to the following sizing of the airplane based on take-off distance requirements:



5.3 Landing Distance

The total landing distance S_L is related to the landing ground run S_{LG} in the following equation:

$$S_L = 1.938 S_{LG} \quad \text{where } S_L \text{ and } S_{LG} \text{ are defined in table 7, appendix A.}$$

Similarly, statistical data obtained from propeller-driven, FAR23 airplanes suggest the following relation between S_{LG} and the stall velocity of the airplane in the

landing configuration, V_{SL} :

$$S_{LG} = 0.265 V_{SL}^2$$

By combining these two equations, a relation between V_{SL} and S_L can be obtained:

$$S_L = 0.5136 V_{SL}^2$$

$$\text{where } V_{SL}^2 = \sqrt{\frac{2 \frac{W}{S}}{\rho CL_{max}}}$$

from this equation relating velocity, lift and wing loading of the airplane, the following relations using three possible lift coefficients for the landing configuration are given:

CL _{max} _L	(W/S) _T ₀
1.4	0.6848 5
1.6	0.7826 86
1.8	0.8805 22

It must be clarified that these results are based on a hypothetical runway 4,000 ft long.

5.4 Speed Constraints

Cruise speed sizing

Requirements:

$V_{cr} = 300 \text{ mph}$ (this corresponds to $M=0.55$ in the low Reynolds number atmosphere of Mars)

$$h_{cr} = 95,144 \text{ ft}$$

$$\sigma = 0.01724$$

The power index I_p can be calculated as:

$$I_p = \sqrt[3]{\frac{\frac{W}{S}}{\sigma \frac{W}{P}}} \text{ where } I_p \propto V_{cr}$$

$$\frac{W}{S}$$

$$\downarrow$$

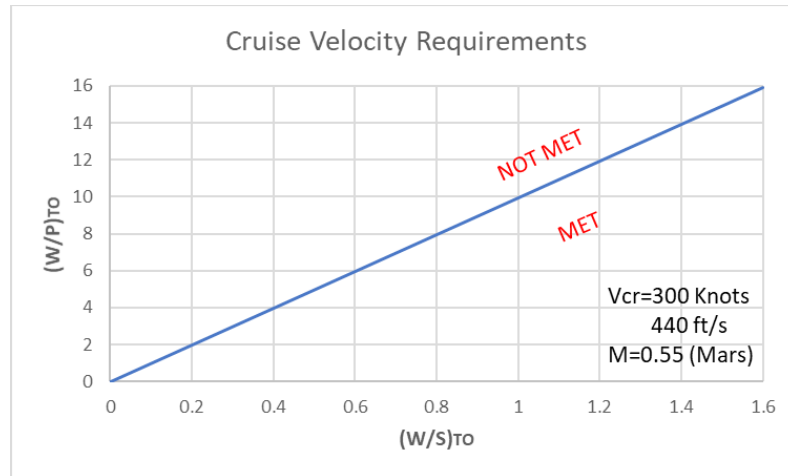
$$\downarrow$$

$$\downarrow$$

$$\downarrow$$

$$\downarrow$$

$$\left(\frac{W}{P}\right)_{\text{to}} = \downarrow$$



5.5 Drag Polar Estimation

For low speed, subsonic airplanes, the drag coefficient can be estimated as:

$$C_D = C_{D_0} + \frac{C_L^2}{\pi A e}$$

Where the zero-lift drag coefficient C_{D_0} can be obtained using the method by

*Lofting*²⁷ using speed and power data:

$$V = 77.3 \sqrt[3]{\frac{\eta_p \frac{W}{S}}{\sigma C_D \frac{W}{P}}}$$

Which can be rewritten using the equation for I_p as:

$$\frac{I_p}{V} i^3$$

$$C_D = 77.3^3 \eta_p i$$

Where $I_p = 1.8$ (for $V_{cr} = 300$ mph, cantilever wing, retractable landing gear)

Assuming $\eta_p = 0.85$ (cruise flight) and $C_{D_o} = 0.9 C_D$, obtain:

$$\frac{1.8}{300} i^3$$

$$\frac{I_p}{V} i^3 = 1.114 * 10^5 i$$

$$C_{D_o} = 1.114 * 10^5 i$$

$$C_{D_o} = i \quad \underline{0.024}$$

Calculation of the drag coefficient for the clean, take-off and landing configurations:

$$C_D = C_{D_o} + \frac{C_L^2}{\pi A e}$$

$$C_{D_o} = 0.024$$

$$A = 37$$

The following statistical values for ΔC_{D_o} and e can be used to calculate the drag polars of the airplane for the clean, take-off and landing configurations with landing gear extended/retracted:

clean	ΔC_{D_o}	0
	e	0.85
TO flaps	ΔC_{D_o}	0.015
	e	0.8
LND flaps	ΔC_{D_o}	0.065
	e	0.75

Land. Gear	ΔC_{D0}	0.02
------------	-----------------	------

Table 11. Statistical values for ΔC_{D0} and e for different flap settings

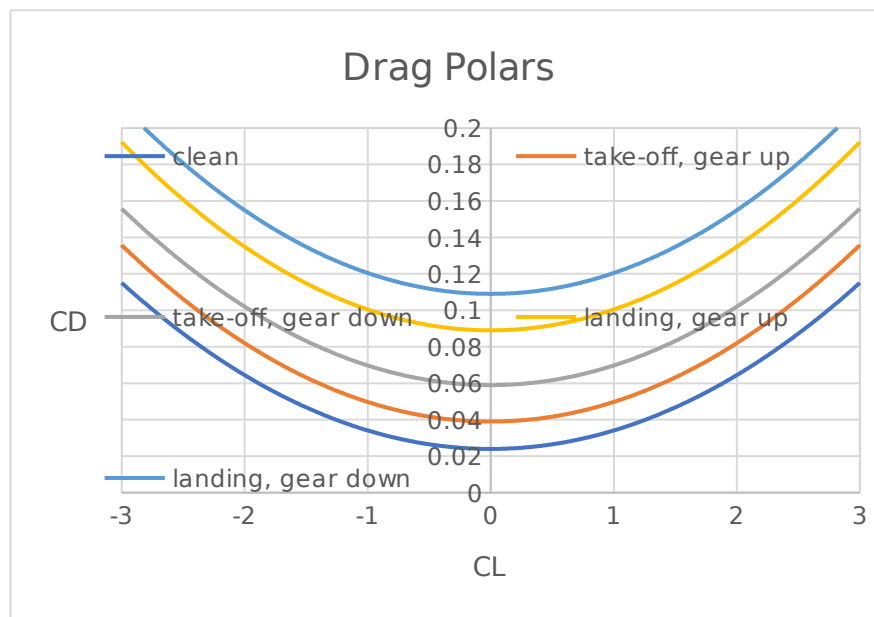
clean configuration: $C_D = 0.024 + 0.01012 C_L^2$

take-off (gear up): $C_D = 0.039 + 0.01075 C_L^2$

take-off (gear down): $C_D = 0.059 + 0.01075 C_L^2$

landing (gear up): $C_D = 0.089 + 0.01147 C_L^2$

landing (gear down): $C_D = 0.109 + 0.01147 C_L^2$



Graph 6. Drag polars

5.6 Climb Constraints

Sizing of the airplane to rate-of climb requirements follows the methodology by Loftin. In this analysis, a desired climb rate of 200 fpm will be considered

Requirements

*all engines operative (AEO)
gear up, take-off flaps
maximum continuous power on all engines
 $RC \geq 200$ fpm*

The rate of climb of the airplane can be represented as:

$$RC = \frac{dh}{dt} = 33,000 RCP$$

$$RCP = \frac{RC}{33,000} = \frac{200}{33,000} = 0.0061 \frac{hp}{lbs}$$

Alternatively, the rate of climb parameter RCP is given by

$$RCP = \frac{\eta_p}{\frac{W}{P}} - \frac{\sqrt{W/S}}{19 \frac{\sqrt{C_L^3}}{C_D} \sqrt{\sigma}}$$

therefore,

$$RC = 33,000 \frac{\eta_p}{\frac{W}{P}} - \frac{\sqrt{W/S}}{19 \frac{\sqrt{C_L^3}}{C_D} \sqrt{\sigma}}$$

maximization of the airplane's rate of climb yields

$$\frac{\sqrt{C_L^3}}{C_{D_{max}}} = 1.345 \sqrt[4]{\frac{Ae}{\sigma}}$$

For estimation purposes, a propeller efficiency for the take-off configuration

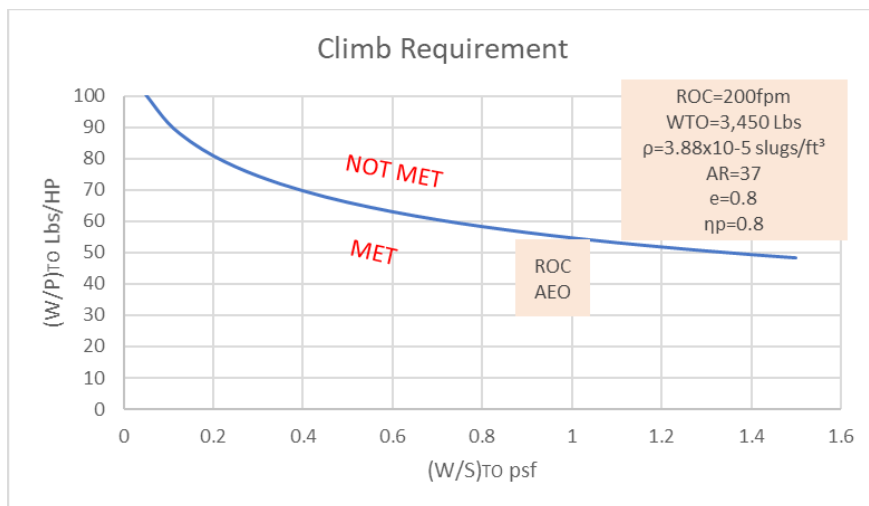
$\eta_{p_o} = 0.8$ and Oswald efficiency factor $e = 0.8$ will be assumed.

The zero-lift coefficient for the climbing stage with take-off flaps on was previously calculated as:

$$C_{D_o,climb} = C_{D_o} + \Delta C_{D_o_i} = 0.024 + 0.015 = 0.039$$

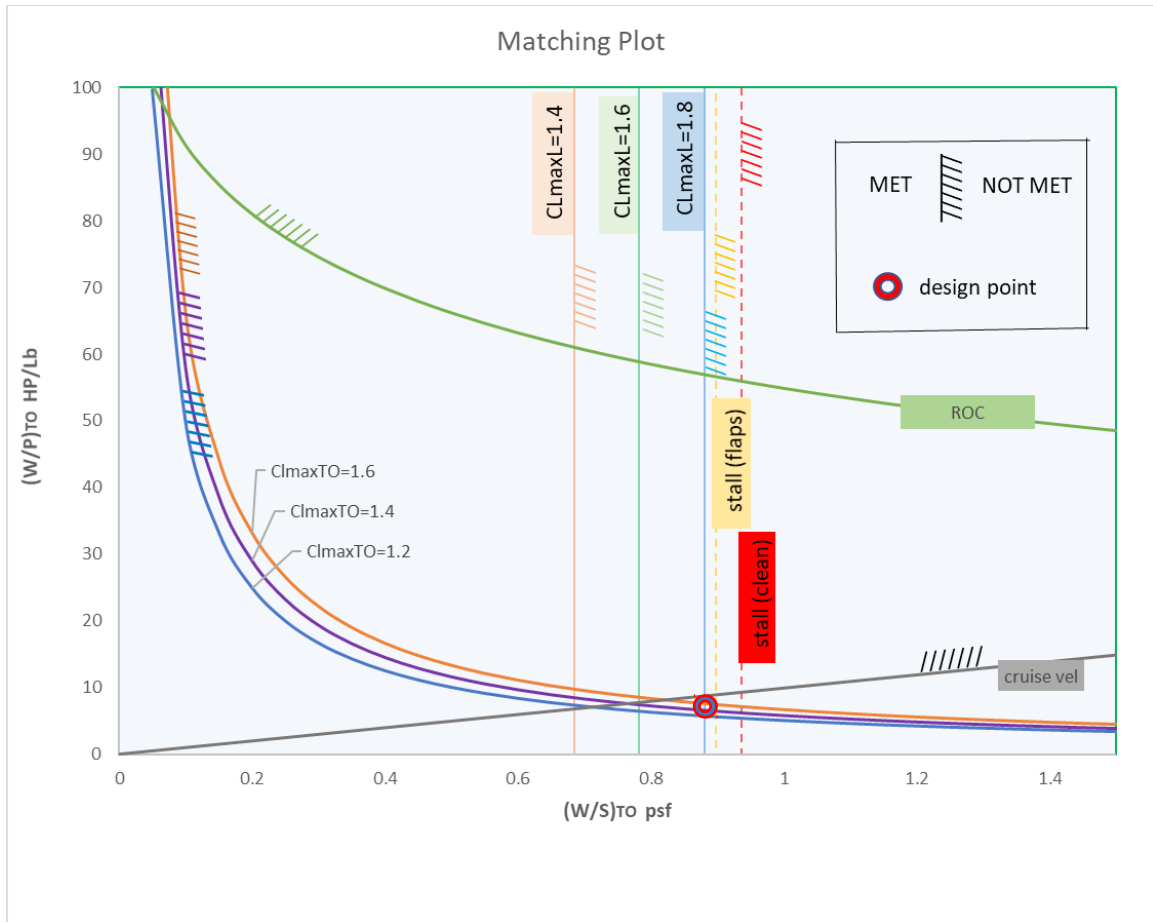
$$\frac{\sqrt{C_L^3}}{C_{D \max}} = 1.345$$

by replacing this value into RCP , it is possible to represent the rate-of-climb (in fpm) of the airplane as a function of wing loading, power loading, propeller efficiency, density, as well as lift and drag coefficient.



Graph 7. Rate of climb requirements

5.7 Matching Plot



Graph 8. Matching plot.

Design point:

$$\left(\frac{W}{S}\right)_i = 0.90 \frac{Lb}{ft^2} \left(\frac{W}{P}\right)_i = 6.98 \frac{Lb}{HP}$$

6. Configuration of the Propulsion System

The power output needed to satisfy the stall, take-off distance, landing distance, cruise velocity and climb requirements is the result of the power loading.

6.1 Engine

The power required per engine can be approximated from the power loading

$$\left(\frac{W}{P}\right)_i = 6.98 \frac{Lb}{Hp}$$

where the gross take-off weight MTOW was previously calculated as:

$$W_i = 3,450 \text{ lbs (weight as measured on Earth)}$$

Correcting MTOW for Mars gravity yields:

$$W_i = 3,450 * 0.377 = 1,300 \text{ Lbs (weight as measured on Mars)}$$

therefore, the powerplant power output required at take-off is:

$$P_i = \frac{W_i}{7.3} = \frac{1,300 \text{ Lbs}}{6.98 \frac{\text{Lb}}{\text{HP}}} = 186 \text{ hp}$$

$$P_i = 180 \text{ hp} = 139 \text{ kW}$$

$$P_{eng} = 93 \text{ hp} = 70 \text{ kW}$$

6.2 Propellers

Propeller diameter

$$D_p = \sqrt{\frac{4 P_{max}}{n_{bl} \pi P_{bl}}}$$

where P_{bl} is the propeller power loading per blade. Typical values are in the order

$$\text{of } 1 - 4 \frac{\text{hp}}{\text{ft}^2} \text{ (single and twin engines) at sea level.}$$

High-altitude propeller design has shown that for a given rpm setting at an altitude of 80,000 ft, the power absorbed by the propeller and transferred to the airstream is 1/30th that at sea level. Assuming a proportional decrease in both the disk loading

and blade loading of the propeller, possible P_{bl} values at the projected low Reynolds number are now used to estimate prospective propeller diameters:

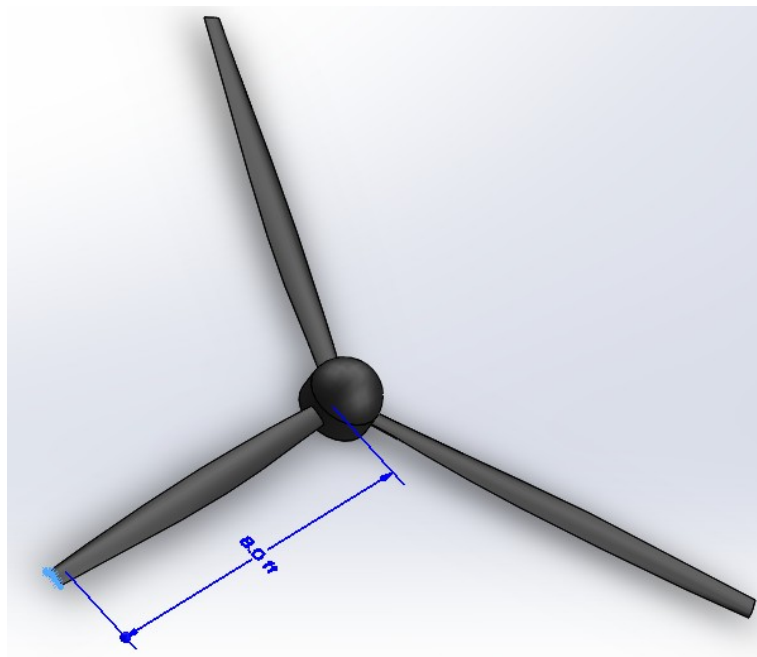
$$\text{number of blades : } n_{bl} = 3$$

$$P_{max} = 93 \text{ hp}$$

P _{bl} (hp/ft ²)	D _p (ft)
0.01	61.9
0.05	27.7
0.1	19.6
0.15	16.0
0.2	13.8
0.25	12.4
0.3	11.3
0.35	10.5
0.4	9.8
0.45	9.2
0.5	8.8

Table 12. Propeller diameter vs. blade load.

In order to maximize the propeller's thrust generation, it is desirable to maximize the propeller diameter. Assuming $P_{bl}=0.15$, a propeller of diameter 16 ft is optimal.



CAD drawing 1. Propeller sizing

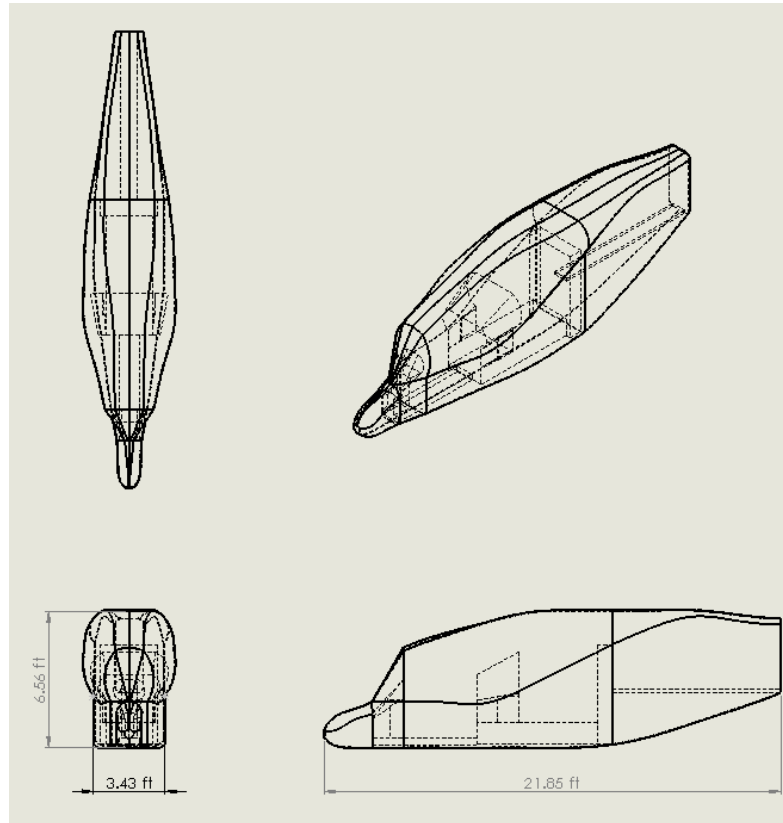
7. Fuselage Design

The dimensions and layout of the fuselage obey volumetric and visibility requirements. In addition to the payload, which includes a low-altitude camera and a cargo of survival equipment, the cabin must be capable of carrying two crewmembers comfortably in a tandem seating arrangement.

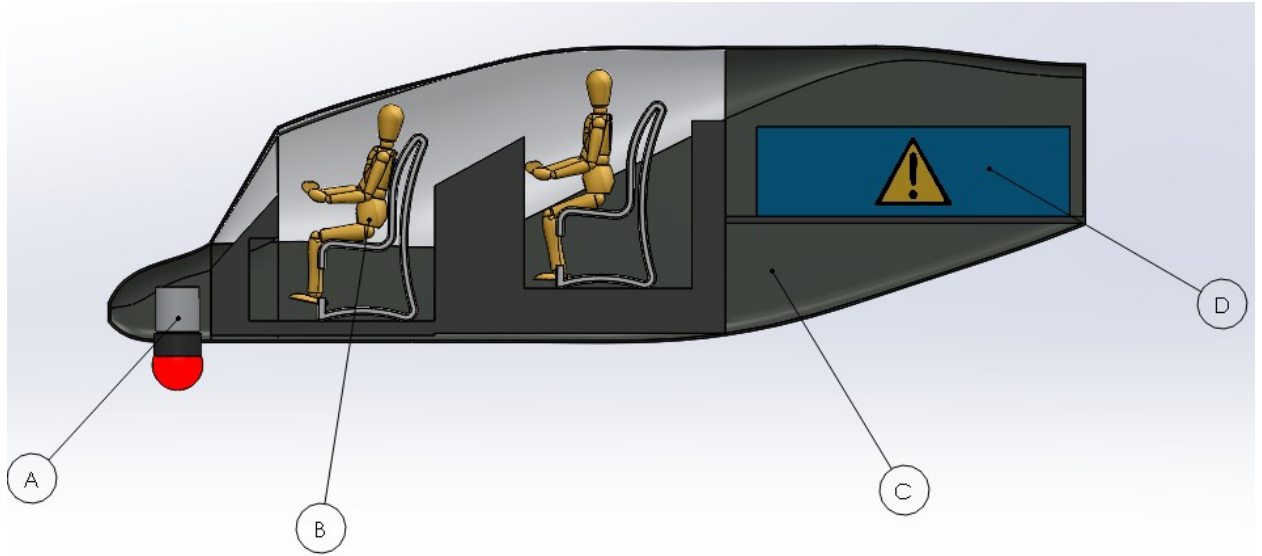
Visibility requirements

Due to the operational nature of the airplane as described in the mission profile, good visibility is essential. Typical vertical inclination visibility as measured from the axis of vision require 15° down and 20° up of visibility.

The following fuselage is designed satisfy volumetric and visibility requirements:

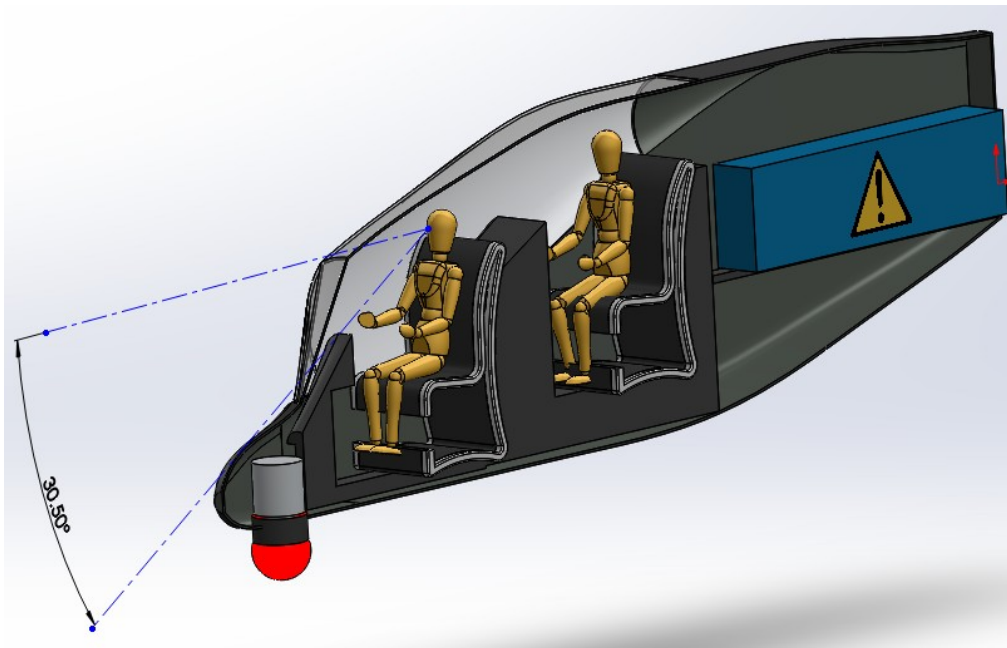


Graph 9. Fuselage dimensions.

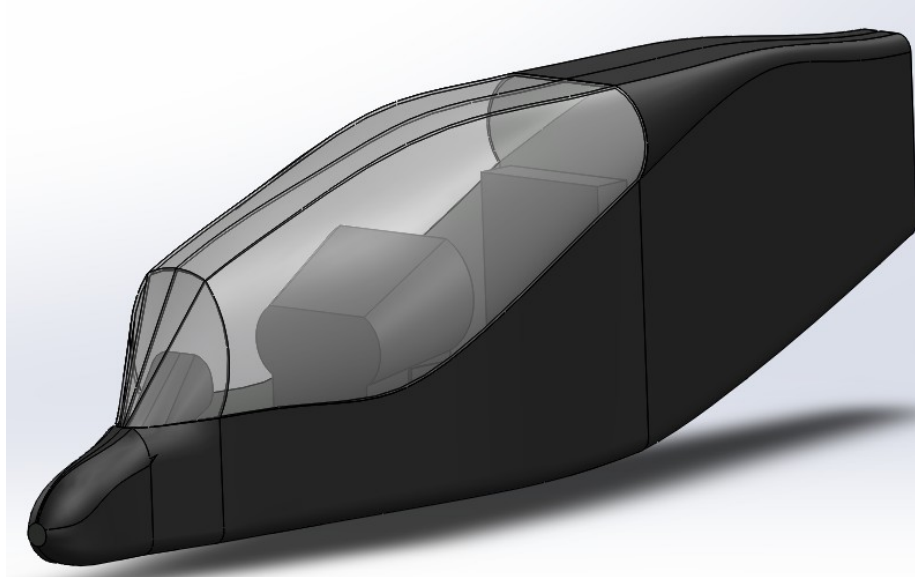


CAD drawing 2. Fuselage layout and payload arrangement.

- A: low-altitude camera*
- B: 5.8 ft tall pilot*
- C: nose wheel well*
- D: cargo*



CAD drawing 3. Cockpit visibility



CAD drawing 4. Complete fuselage design.

8. Wing Sizing

Because of the required clearance between the propeller and the ground, a high wing configuration is convenient. Due to the projected high aspect ratio, a strutted or braced wing can be considered.

$$\frac{W}{S}$$

$$W_{\zeta} = 1,300 \text{ lbs}$$

$$S_w = 1,445 \text{ ft}^2$$

$$A = 37 \text{ (assumed)}$$

$$b = \sqrt{S_w A} \quad \zeta \sqrt{1,445 * 37} = 231 \text{ ft}$$

This wing span clearly indicates that a structure that can support the weight of the wing is necessary. Two possibilities for this structural support will be considered in the final design of the wing; a strut connecting the wing to the fuselage, or a vertical strut mounted near the wing tip.

Assuming a taper ratio $\lambda=0.4$, and a root cord length $c_r=8.4\text{ft}$ which fits the dimensions of the fuselage, obtain,

$$\lambda = \frac{c_t}{c_r} \rightarrow c_t = \lambda c_r = 0.4 * 8.4 = 3.36$$

knowing $c_t; c_r \wedge \lambda$, mean aerodynamic chord is determined as:

$$MAC = \frac{2}{3} c_r \frac{1+\lambda+\lambda^2}{1+\lambda} \quad ; \quad \frac{2}{3} * 8.4 \frac{1+0.4+0.4^2}{1+0.4} = 6.25\text{ft}$$

$$\Lambda_{i/TE} = \tan^{-1} \frac{\frac{1}{2}(c_r - c_t)}{\frac{b}{2}} \quad ; \quad \tan^{-1} \frac{\frac{1}{2}(8.4 - 3.36)}{\frac{231}{2}} = \pm 1.25$$

$$\Lambda_{\frac{c}{4}} = \tan^{-1} \frac{\frac{1}{4}(c_r - c_t)}{\frac{b}{2}} \quad ; \quad \tan^{-1} \frac{\frac{1}{4}(8.4 - 3.36)}{\frac{231}{2}} = 0.63^\circ$$

The required lift coefficient for cruise flight at the expected velocity, weight and air density conditions can be estimated as:

$$C_{L_{cr}} = \frac{W_i - 0.4 W_F}{\dot{q} S_w} \quad ; \quad \frac{1,300 - 0.4(5.73)}{\frac{1}{2} * 0.0000388 * 440 * 1,445} = 0.19$$

this corresponds to a cruise velocity of 260 knots = 440 ft/s (IAS and TAS) or M=0.55 near the surface of Mars.

Selection of the airfoil

The lift and drag properties of several airfoils were analyzed. Due to the low density, low Reynolds number and high Mach number characteristics of Mars, it is critical to have access to an airfoil capable of generating a sufficient high lift coefficient with minimal drag.

High-altitude airfoils like the Douglas Liebeck LNV109a and the Apex-16. specially designed for low Reynolds were tested using Xfoil.

Airfoil analysis

Aerodynamic results for the LNV109a, Apex-16, and NACA 4415 airfoils are summarized next. The initial conditions given for the numerical analyses include:

$$\rho = 0.0000388 \frac{\text{slugs}}{\text{ft}^3}$$

$$\nu = 0.011698 \frac{\text{ft}^2}{\text{s}} \text{ (kinematic viscosity)}$$

$$l = 6.25 \text{ ft (MAC)}$$

$$V_{s_1} = 186 \frac{\text{ft}}{\text{s}} \text{ (stall velocity in the clean configuration)}$$

stall velocity in the landing configuration

$$V_{s_0} = 160 \frac{\text{ft}}{\text{s}} \text{ ()}$$

flapping location = 0.8 c

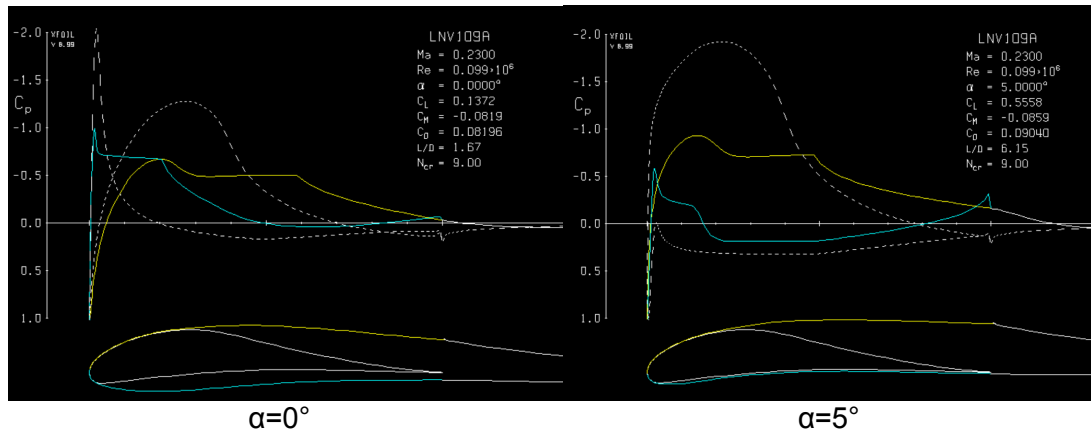
$$\mathfrak{R} = \frac{\rho v l}{\mu} = \frac{v l}{\nu}$$

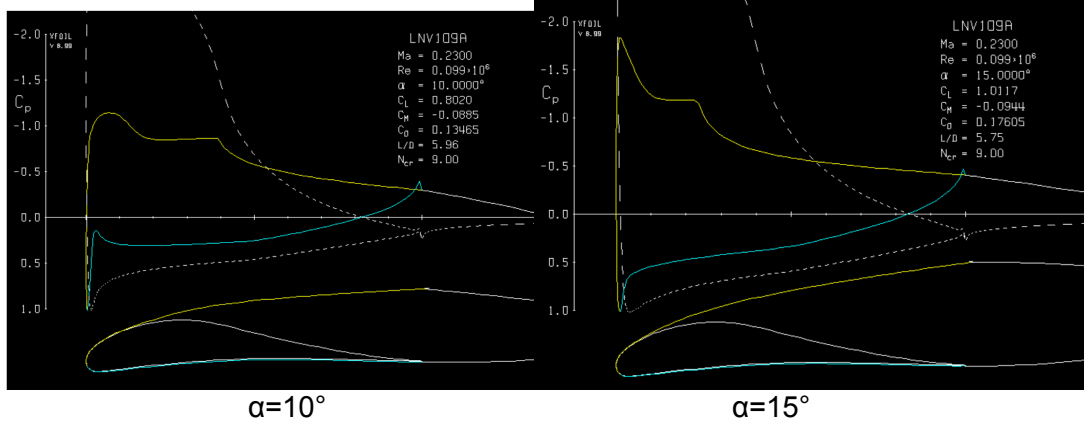
$$\mathfrak{R}_{\text{clean}} = \frac{186 * 6.25}{0.011698} = 99,200$$

$$\mathfrak{R}_{\text{Landing}} = \frac{160 * 6.25}{0.011698} = 85,700$$

Douglas Liebeck109a (LNV109a)

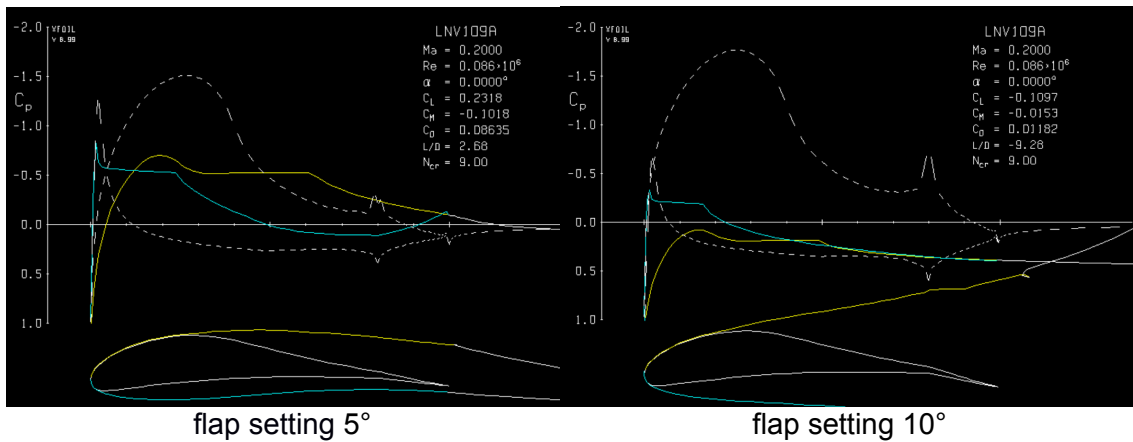
LNV109a in the clean configuration. ($V_{s_1}, M = 0.23, \mathfrak{R} = 99,200, \text{power off } \hat{i}$)





Simulation for the clean configuration indicates a complete stall of the airfoil at the given conditions, even at the low angle of attack ($\alpha = 0^\circ$) as seen by the airflow separation near the leading edge.

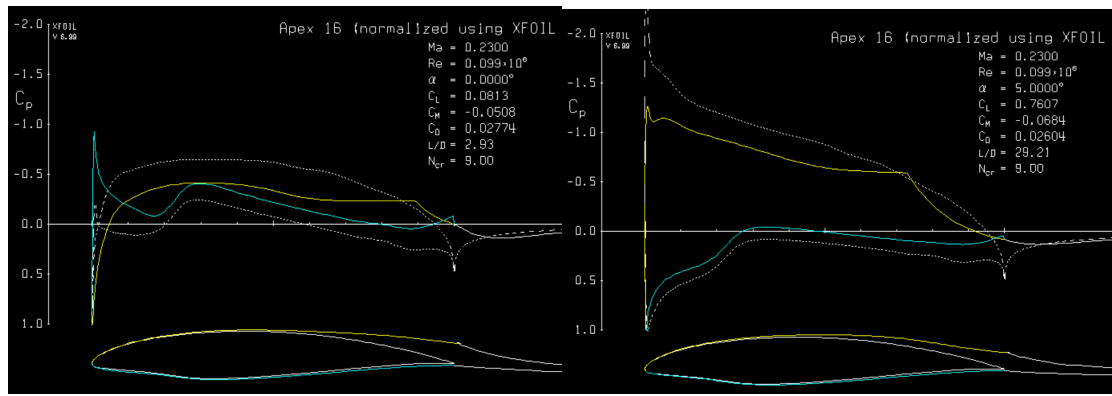
LNV109a in landing configuration. (V_{s_0} , $M=0.2$, $\Re = 86,700$, power off)



Using a 5° flap setting, the simulation shows a similar flow separation with a minor gain in lift coefficient C_L than the clean configuration at the same angle of attack $\alpha=0^\circ$. Further flap deployment indicates no flow reattachment and complete aerodynamic stall.

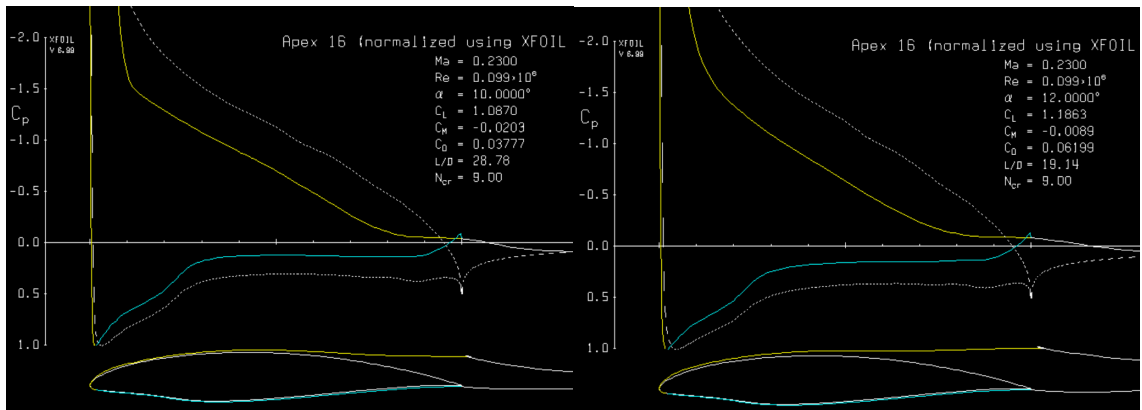
Apex-16

Apex-16 in the clean configuration. (V_{s_1} , $M=0.23$, $\Re = 99,200$, power off)



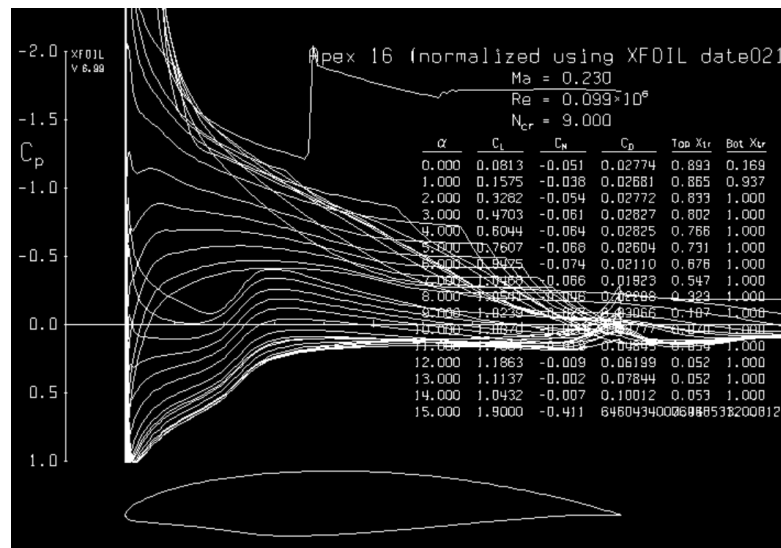
$\alpha=0^\circ$

$\alpha=5^\circ$



$\alpha=10^\circ$

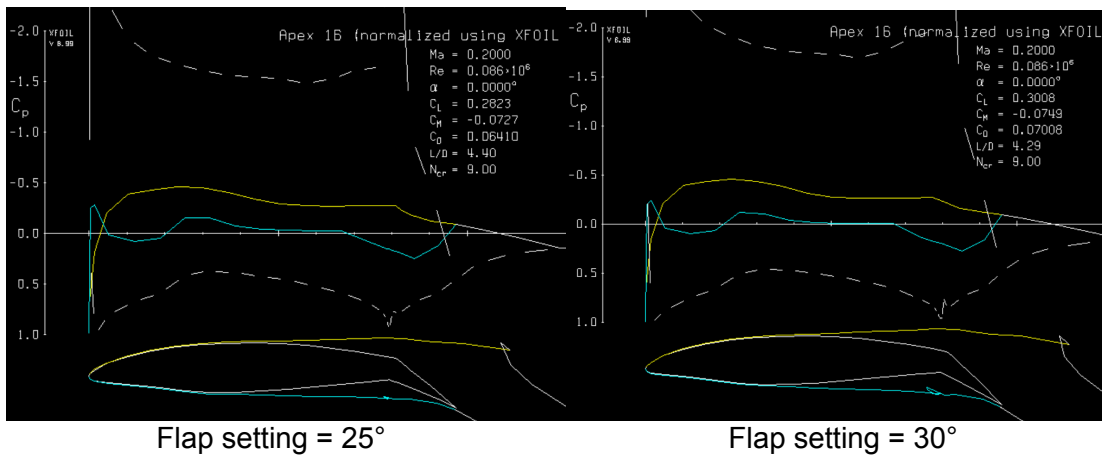
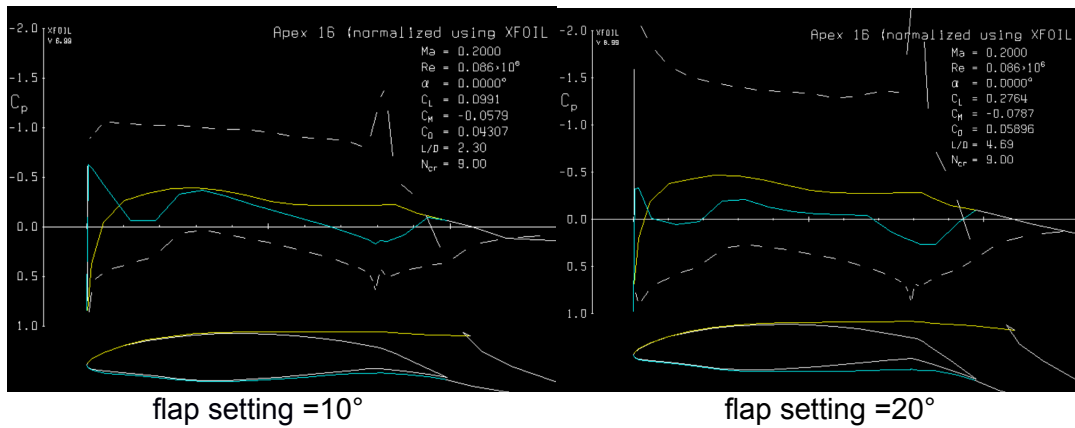
$\alpha=12^\circ$



Aerodynamic analysis of this airfoil with flaps retracted and an angle of attack $\alpha=0^\circ$ show a progressive boundary layer separation until stall occurs at approximately $\alpha=12^\circ$. The maximum lift coefficient generated by the Apex-16 under the given conditions is

$$C_{L_{max}} \approx 1.19$$

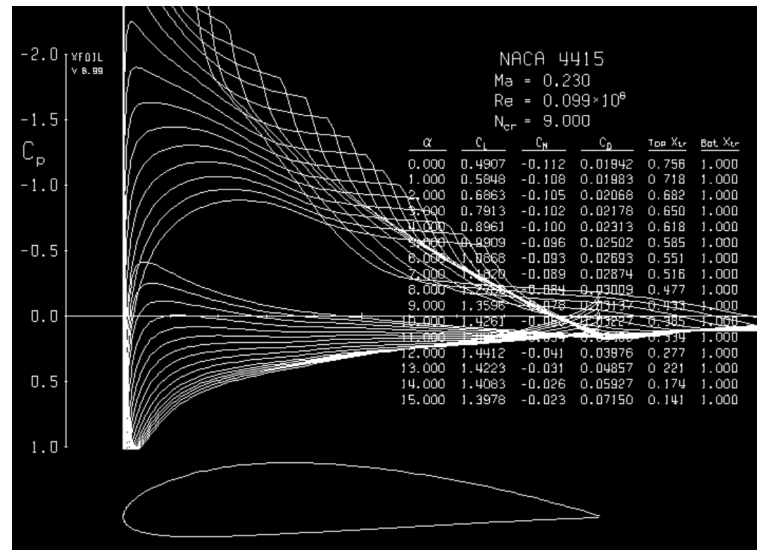
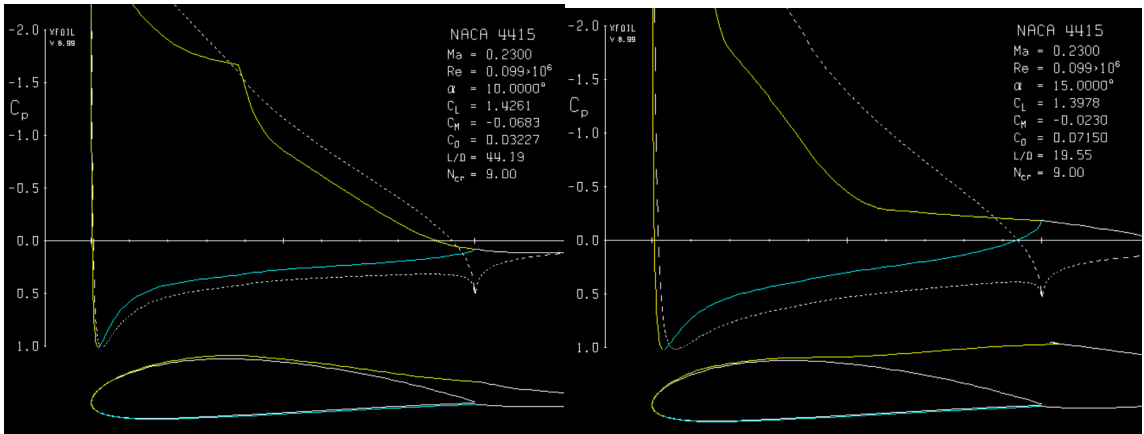
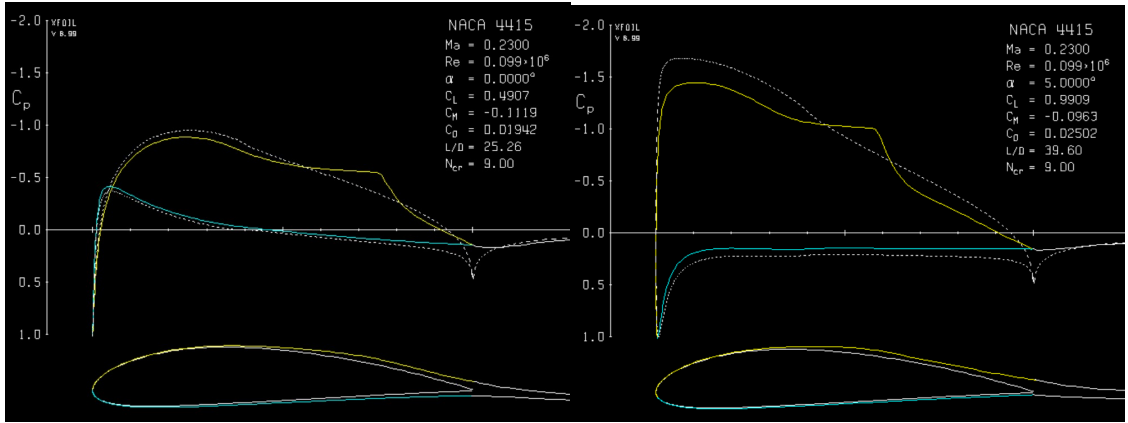
Apex-18 in landing configuration. ($V_{s_0}, M=0.2, \Re = 86,700, \text{power off}$)



Xfoil's prediction for the Apex-16 airfoil at the given conditions shows a maximum lift coefficient $C_{L_{max}} \approx 0.3$. This indicates that the airfoil has an adverse reaction to flap inputs at the given Reynolds number.

NACA 4415

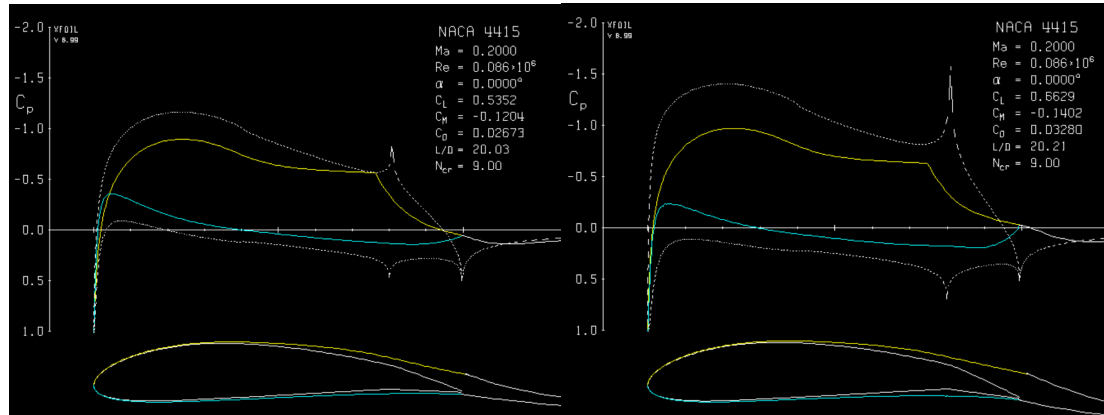
NACA 4415 in the clean configuration. ($V_{s_1}, M=0.23, \Re = 99,200, \text{power off}$)



Predictions for the NACA 4415 in the clean configuration indicate better aerodynamic characteristics than both the LNV109a and the Apex-16 in response to the challenging conditions. Due to the characteristic shape of this airfoil, there is more a gradual airflow

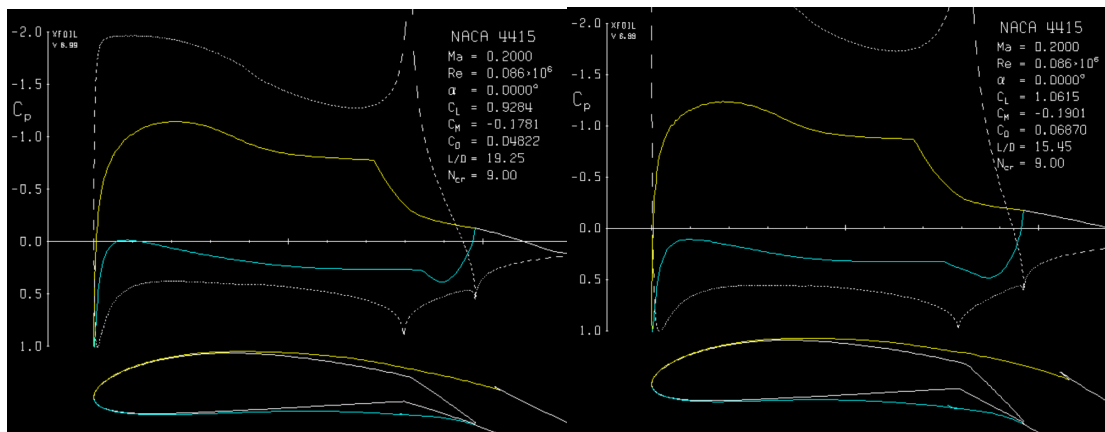
separation at both the top and bottom surfaces of the airfoil. The maximum lift coefficient obtained is ≈ 1.44 at about $\alpha = 12^\circ$.

NACA 4415 in landing configuration. ($V_{s_0}, M=0.2, \mathcal{R}=86,700$, power off \hat{i})



flap setting = 5°

flap setting = 10°



flap setting = 20°

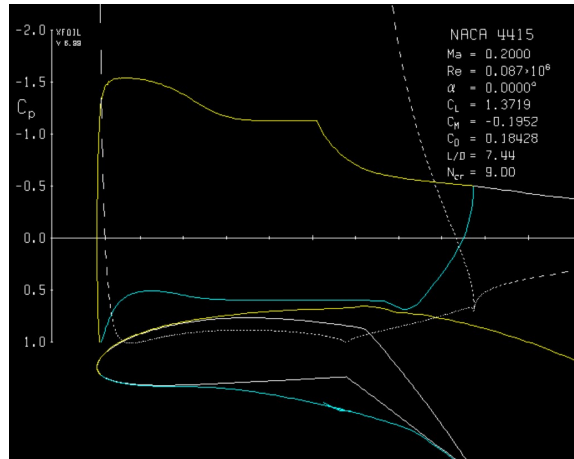
flap setting = 30°

Although the coefficient of lift generated by the NACA 4415 is enhanced by the input of flaps, reaching substantial higher $C_{L_{max}}$ than both the LNV109a and Apex-16 airfoils,

it doesn't reach the required value of $C_{L_{max}} = 1.8$ previously considered in the calculation, which corresponds to an input in angle of attack $\alpha = 0^\circ$.

Optimization of the NACA 4415:

Increased values of $C_{L_{max}}$ can be generated by changing the flap hinge location. For instance, using a flap setting of 40° , a $C_{L_{max}} = 1.37$ could be generated using the reference angle of attack $\alpha = 0^\circ$ at a hinge location of 60% chord (0.6c) as shown below:



CFD analysis of the NACA 4415

A numerical simulation of the aerodynamic characteristics of the NACA 4415 in order to predict the boundary layer separation on a potential 3d wing at increasing angles of attack.

Initial conditions

100% CO_2 atmosphere

Steady state

Turbulent flow using the Spalart-Allmaras Turbulence model in a Reynolds-Averaged Navier-Stokes (RANS) form

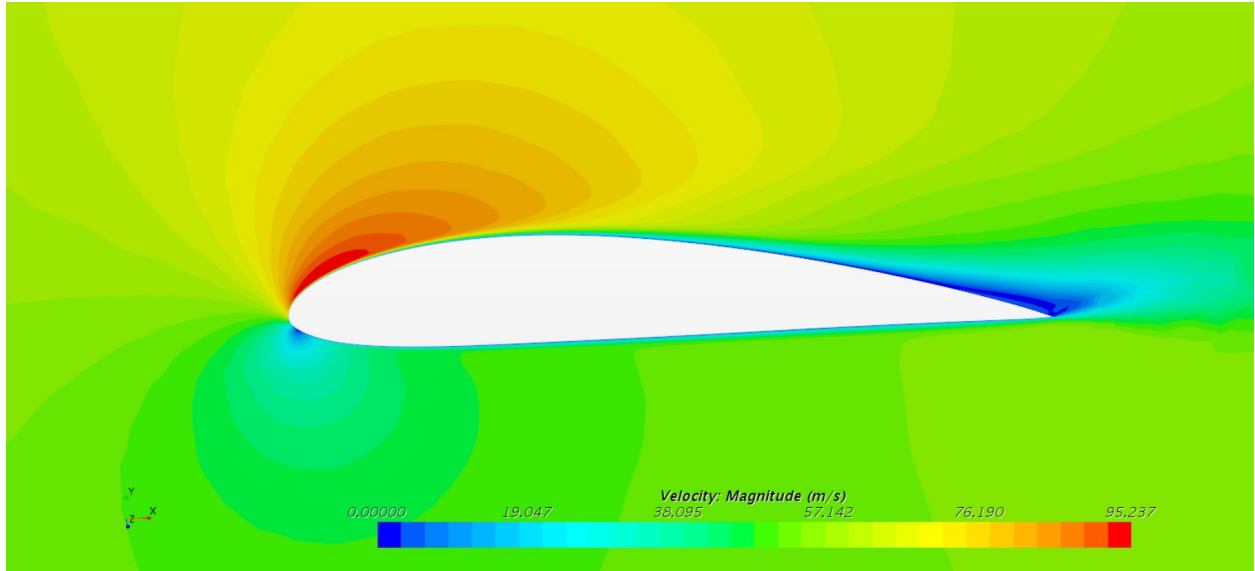
Velocity = 57 m/s - constant

Density = 0.02 kg/m³ - constant

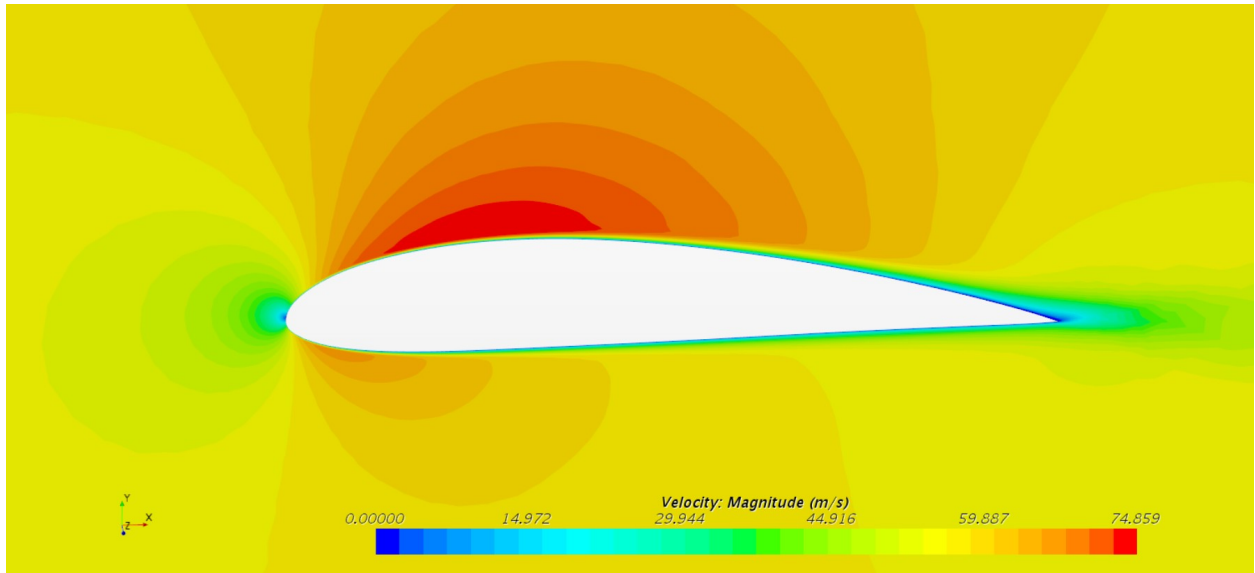
Dynamic viscosity = 1.42e-05 Pa-s - constant

Reference pressure = 600 Pa, Initial pressure = 0 Pa

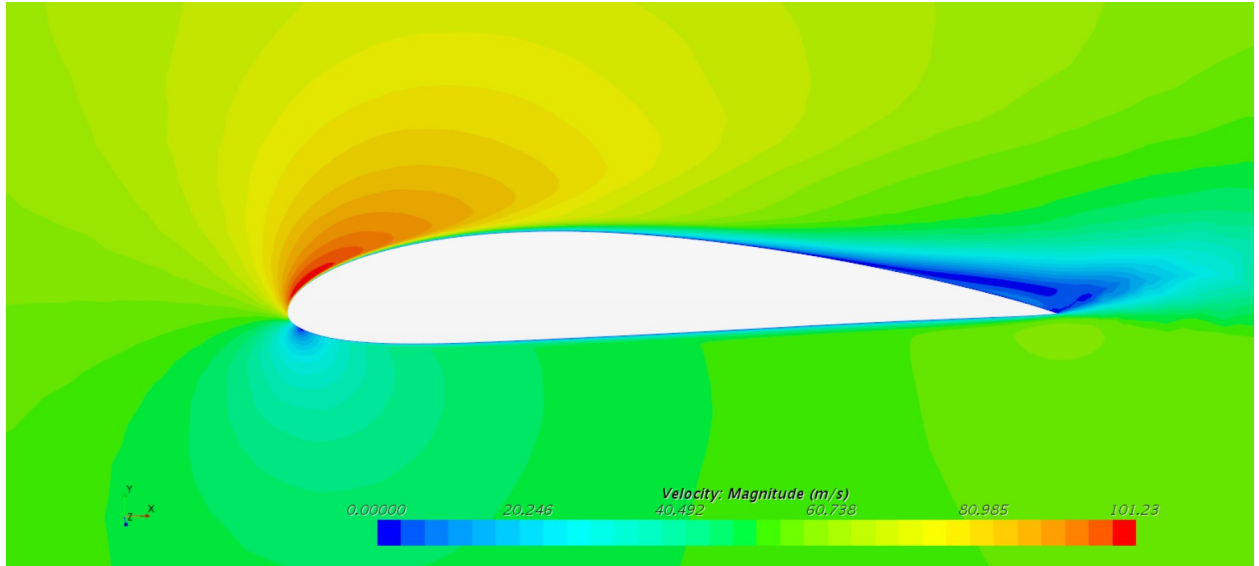
Results correspond to four different angles of attack $\alpha = 0^\circ, 10^\circ, 12^\circ$ and 15° .



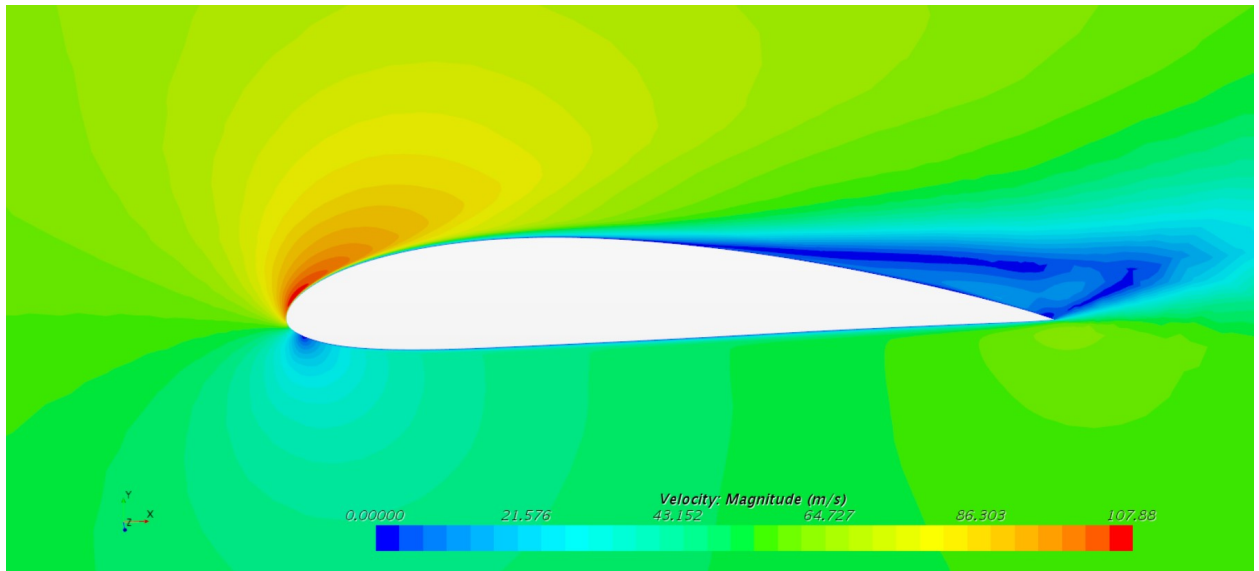
$\alpha = 0^\circ$



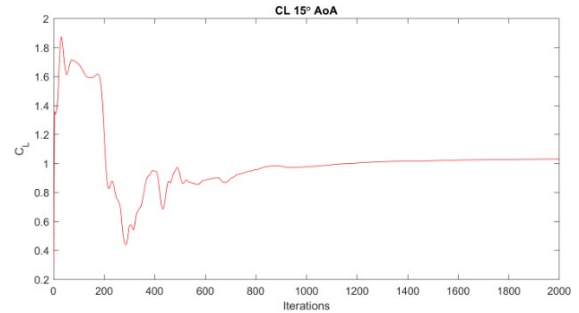
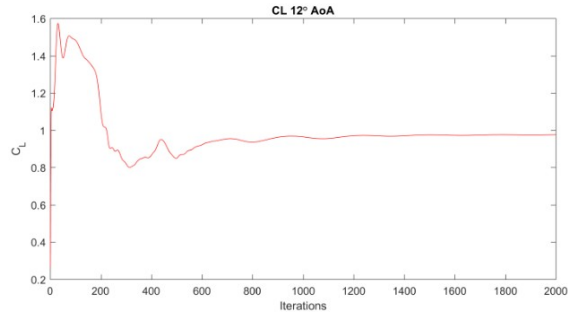
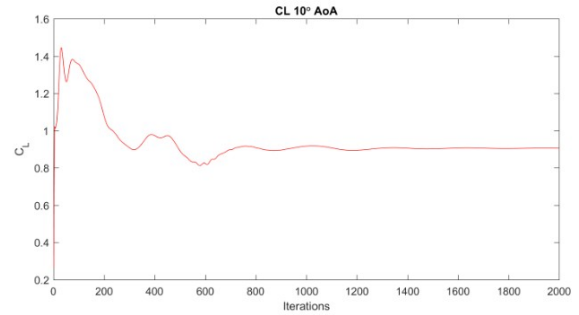
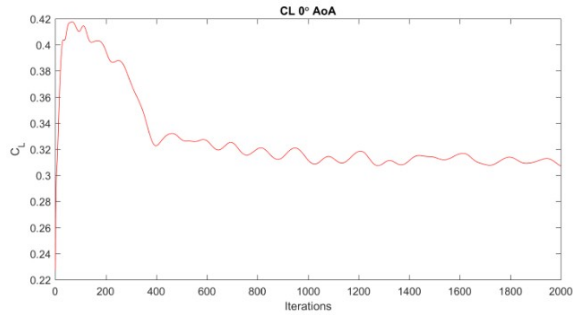
$\alpha = 5^\circ$



$\alpha = 12^\circ$



$\alpha = 15^\circ$

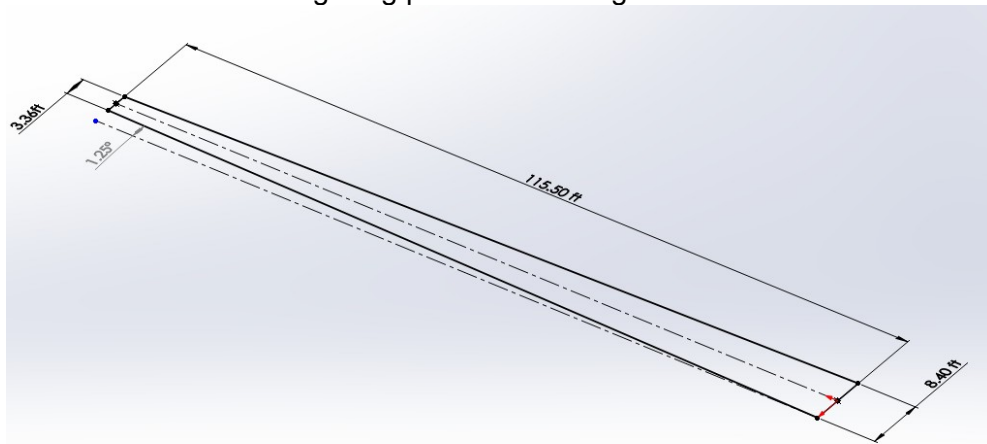


This trend in the separation of the boundary layer as α is increased agrees with the results obtained for the 2D airfoil. The CFD simulation shows how the NACA 4415 responds to angle of attack input at the given flight conditions, with total separation occurring at about $\alpha=10^\circ-12^\circ$, which agrees with the results obtained for the 2d airfoil using Xfoil.

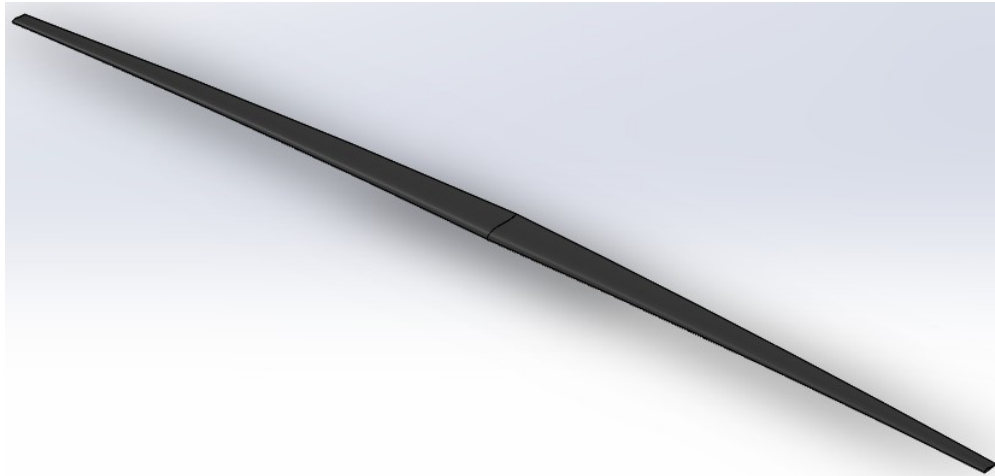
Similar correspondence for the lift coefficients obtained for the 3D wing and 2D airfoil can be seen, with a $C_{L_{max}} \approx 1.6$ for the 3D wing

Wing planform

Based on the required geometrical characteristics of the wing, in addition to the airfoil, the following wing planform is designed:



CAD drawing 5. Wing dimensions



CAD drawing 6. 3D wing

9. Design of the High-Lift Devices

Based on the previous numerical estimation for the aerodynamic performance of the NACA 4415 for the clean and flapped configurations, the following lift coefficients can be considered:

$$C_{L_{max}} = 1.45$$

$$C_{L_{max_i}} = 1.6$$

$$C_{L_{max_e}} = 1.8$$

It is necessary to verify, however, that the wing planform just designed can generate a three-dimensional lift coefficient that is consistent with the $C_{L_{max}}$ value generated by the NACA 4415 airfoil.

$$C_{L_{max_e}} = 1.05 C_{L_{max}} \quad (\text{for long-coupled airplanes with } \frac{l_h}{c} > 5.0)$$

$$C_{L_{max_e}} = 1.05 * 1.45 = 1.5225$$

Correcting for the effect of sweep angle (Λ) on the 3-D wing, obtain,

$$C_{L_{max_e, i_{unswept}}} = \frac{C_{L_{max_e, swept}}}{\cos \Lambda_{c/4}} \quad i_{\frac{1.52}{\cos(0.625^\circ)}} = 1.5226$$

To verify that the wing can generate this value,

$$C_{L_{max_w}} = k_\lambda \frac{C_{L_{max_r}} + C_{L_{max_t}}}{2} \quad \text{where } k_\lambda = 0.95 \text{ for } \lambda = 0.4$$

$$C_{L_{max_r}} + C_{L_{max_t}} = \frac{2 * 1.5}{0.95} = 3.1$$

This is the required $C_{L_{max_w}}$ that must be generated by the root and tip airfoils combined.

Assuming the use of NACA 4415 airfoils at both the root and the tip,

$$\Re_r = \frac{\rho V c_r}{\mu} = \frac{3.88 * 10^{-5} * 8.4}{1.53 * 10^{-4}} = 201,000$$

$$\Re_t = \frac{\rho V c_t}{\mu} = \frac{3.88 * 10^{-5} * 3.36}{1.53 * 10^{-4}} = 80,200$$

Using Xfoil, maximum lift coefficients can be obtained for both airfoils at their respective Reynolds numbers,

$$C_{L_{max_r}} = 1.47$$

$$C_{L_{max_t}} = 1.44$$

$$\text{Therefore, } C_{L_{max_r}} + C_{L_{max_t}} = 1.47 + 1.44 = 2.91$$

$$\text{This is about 6\% of the required } C_{L_{max_r}} + C_{L_{max_t}} = 3.1.$$

It is recommended that the difference between these values be within 5%, otherwise redesign of the wing planform must be performed.

Determination of required incremental lift coefficient to be generated by the flaps can be obtained as:

$$\Delta C_{L_{max_r}} = 1.05(C_{L_{max_r}} - C_{L_{max_t}}) \quad \hat{=} 1.05 * (1.6 - 1.45) = 0.16$$

$$\Delta C_{L_{max_t}} = 1.05(C_{L_{max_t}} - C_{L_{max_r}}) \quad \hat{=} 1.05 * (1.8 - 1.45) = 0.37$$

The required section lift coefficient with flaps down can be calculated as:

$$\Delta C_{L_{max}} = \frac{\Delta C_{L_{max}} \frac{S_w}{S_{wf}}}{k_A} \quad \text{where } S_{wf} \text{ is the flapped wing area}$$

$$k_A = \frac{1 - 0.08 \cos^2 \Lambda_c \frac{\Lambda_c}{4}}{\cos^{(\frac{3}{4})}(\frac{\Lambda_c}{4})} = \frac{1 - 0.08 \cos^2 0.62}{\cos^{(\frac{3}{4})}(0.62)} = 0.92$$

Assuming arbitrary ratios of wing area to flapped wing area, the following relation is established:

S _{wf} /S		TO flaps	LD flaps
0.3	Δd _{max}	0.57	1.33
0.4	Δd _{max}	0.43	1.00
0.5	Δd _{max}	0.34	0.80
0.6	Δd _{max}	0.29	0.67

Table 13. $\Delta C_{L_{max}}$ requirements for different ratios S_{wf}/S_w .

The required ΔC_L that the flaps must generate for both take-off and landing requirements can be computed as follows:

for estimation purposes, the following flap geometry can be assumed:

$$\frac{Z_{fh}}{c} = 0.1$$

$$\frac{c_f}{c} = 0.25$$

$$\delta_{f_i} = 15^\circ$$

$$\delta_{f_L} = 45^\circ$$

$$\frac{c'}{c} = 1 + 2 \frac{Z_{fh}}{c} \tan\left(\frac{\delta_f}{2}\right)$$

For take-off:

$$\frac{c'}{c} = 1 + 2 \frac{Z_{fh}}{c} \tan\left(\frac{\delta_{f_i}}{2}\right) = 1 + 2 * 0.1 \tan\left(\frac{15^\circ}{2}\right) = 1.03$$

For landing:

$$\frac{c'}{c} = 1 + 2 \frac{Z_{fh}}{c} \tan\left(\frac{\delta_{fL}}{2}\right) = 1 + 2 * 0.1 \tan\left(\frac{45^\circ}{2}\right) = 1.08$$

$$C_{L_{\alpha_i}} = C_{L_{\alpha}} \frac{c'}{c}$$

For take-off:

$$C_{L_{\alpha_i}} = C_{L_{\alpha}} \frac{c'}{c} = 1.03 * 2\pi = 6.45$$

For landing:

$$C_{L_{\alpha_i}} = C_{L_{\alpha}} \frac{c'}{c} = 1.08 * 2\pi = 6.8$$

To calculate the variation in lift coefficient for plain, split and single-slotted flaps:

Plain flaps

$$\Delta C_L = C_{L_{\delta_f}} \delta_f k \quad \text{where } k \wedge C_{L_{\delta_f}} \text{ are obtained } \delta_f \text{ statistical values}$$

Split flaps

$$\Delta C_L = k_f \delta_f \quad \text{where } k_f \wedge \delta_f \text{ are obtained } \delta_f \text{ statistical values}$$

Single slotted flaps

$$\Delta C_L = C_{L_{\alpha}} \alpha_{\delta_f} \delta_f \quad \text{where } \alpha_{\delta_f} \text{ is obtained } \delta_f \text{ statistical values}$$

The following values are now obtained:

Flap type	split	plain	single slot
$\Delta C_{L_{\max to}}$	0.30	0.75	0.89
$\Delta C_{L_{\max in}}$	0.84	1.24	2.11

Table 14. Required variation in lift coefficient for 3 types of flap

Direct comparison to the values obtained in table 14 shows that only the single-slotted flaps meets all the take-off and landing requirements. The requires variation if lift

coefficient for landing is, however, much more than what is required in table 13, therefore landing flaps are not critical.

Using the critical values for take-off $\Delta c_{L_{max}}$, the ratio between the flapped wing area to the wing area can be approximated:

$$\Delta c_{L_{max}} = \frac{\Delta C_{L_{max}} \frac{S_w}{S_{wf}}}{k_{\Lambda}} \rightarrow \frac{S_{wf}}{S_w} = \frac{\Delta c_{L_{max}}}{\Delta C_{L_{max}, k_{\Lambda}}} = \frac{0.16}{0.89 * 0.92} = 0.192$$

$$\frac{S_{wf}}{S_w} = 0.192 \rightarrow S_{wf} = 0.192 * 1,445 f t^2 = 278 f t^2 \rightarrow \frac{S_{wf}}{2} = 139 f t^2$$

Summary of the flap geometry

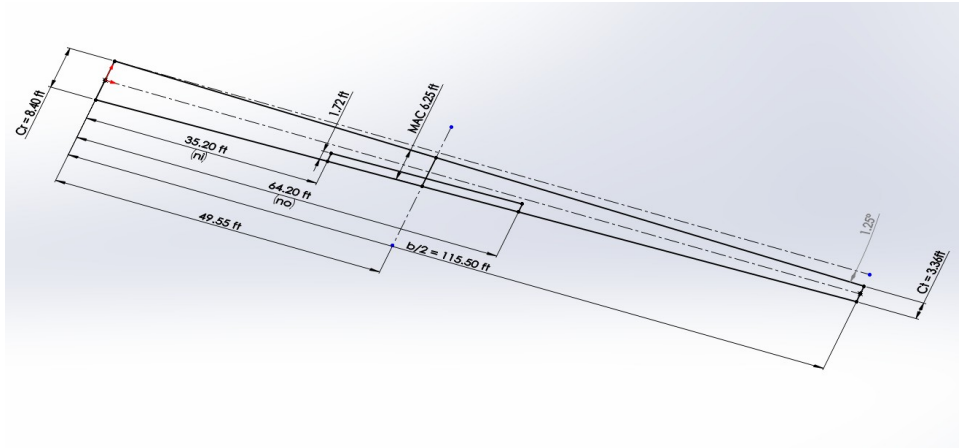
Flap type	single-slotted
S_{wf}/S	0.192
cf/c	0.25
Zh/c	0.1
δ_{fTO}	15
δ_{fL}	45

Table 15. Flap geometry

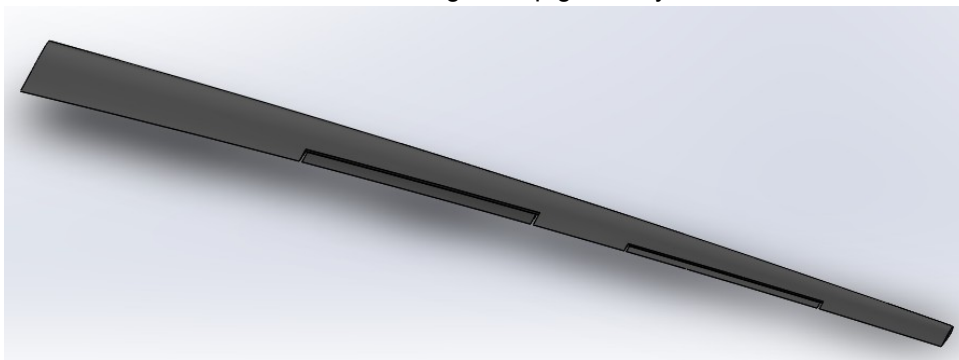
Using the obtained value of $\frac{S_{wf}}{S_w}$, the span stations η_0, η_i are now calculated:

$$\frac{S_{wf}}{S_w} = (\eta_0 - \eta_i) \frac{2 - (1 - \lambda)(\eta_0 + \eta_i)}{1 + \lambda}$$

After assigning a discrete value for the inner span station $\eta_i = 0.15$, the following single-slotted flap is obtained:



CAD drawing 7. Flap geometry



CAD drawing 8. 3D wing and flap geometry

10. Design of the Empennage and the Longitudinal and Directional controls

Sizing of the horizontal and vertical stabilizers

$$x_h = 58 \text{ ft}$$

$$x_v = 58.7 \text{ ft}$$

$$\dot{V}_h = 0.65$$

$$\dot{V}_v = 0.03$$

$$\frac{S_e}{S_h} = 0.3$$

$$\frac{S_r}{S_v} = 0.3$$

Calculation of the surface area of the horizontal and vertical stabilizers

$$S_H = \frac{\dot{V}_h S_w \dot{c}}{x_h} \quad ; \quad \frac{0.65 * 1,445 * 6.25}{58} = 101.2 \text{ ft}^2$$

$$S_V = \frac{\dot{V}_V S_w \dot{c}}{x_V} \quad ; \quad \frac{0.03 * 1,445 * 6.25}{58.7} = 170.8 \text{ ft}^2$$

Using aspect ratios of 5 and 3 for the horizontal and vertical stabilizers, respectively, the following empennage dimensions are determined:

$$A_H = 5$$

$$A_V = 3$$

$$\Lambda_{c/4_H} = \Lambda_{c/4_V} = 0^\circ$$

$$\lambda_H = \lambda_V = 1.0$$

$$i_H = i_V = 0^\circ$$

$$\Gamma_H = 0^\circ$$

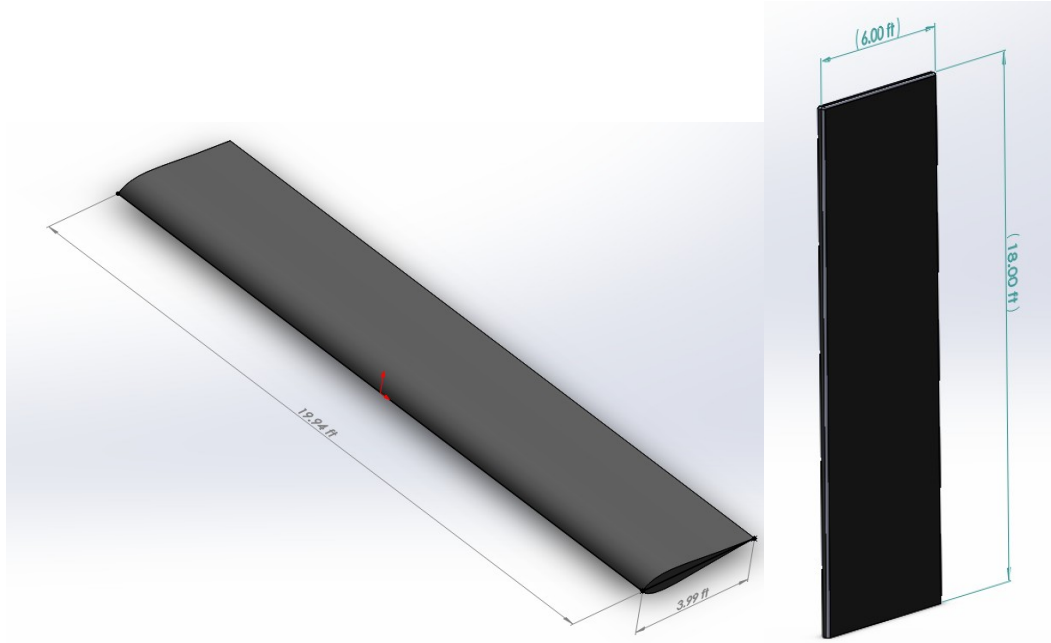
$$\Gamma_V = 90^\circ$$

$$b_H = \sqrt{A_H S_H} = \sqrt{5 * 101.2} = 22.5 \text{ ft}$$

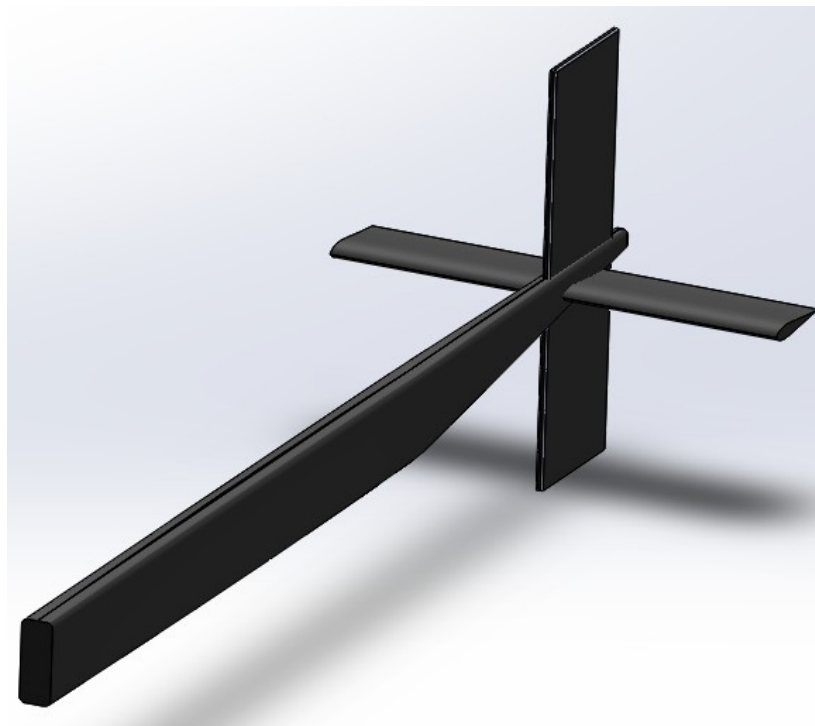
$$b_V = \sqrt{A_V S_V} = \sqrt{3 * 170.8} = 22.6 \text{ ft}$$

$$c_{r_H} = \frac{S_H}{b_H} = \frac{101.2}{22.5} = 4.5 \text{ ft} = c_{t_H}$$

$$c_{r_V} = \frac{S_V}{b_V} = \frac{170.9}{22.6} = 7.54 \text{ ft} = c_{t_V}$$



CAD drawing 9. Horizontal and vertical stabilizers planform



CAD drawing 10. Empennage configuration

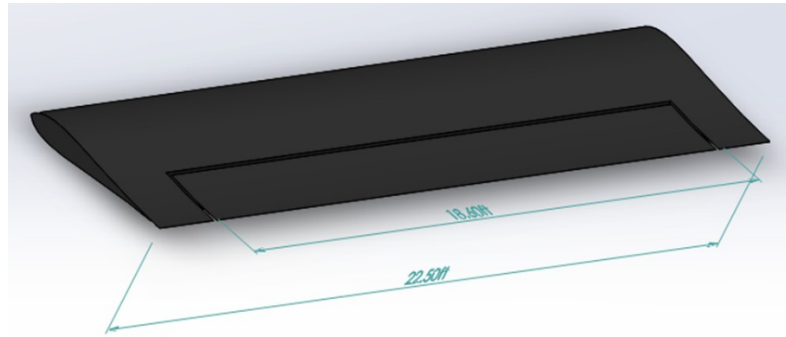
Sizing of the elevator and rudder

$$S_{elev} = S_H \frac{S_e}{S_h} = 101.2 * 0.3 = 30.36 \text{ ft}^2$$

$$S_{rud} = S_V \frac{S_r}{S_v} = 170.8 * 0.3 = 51.24 \text{ ft}^2$$

$$c_{elev} = \frac{S_{elev}}{b_{elev}} = \frac{30.36 \text{ ft}^2}{18.5 \text{ ft}^2} = 1.64 \text{ ft}$$

$$c_{rud} = \frac{S_{rud}}{b_{rud}} = \frac{51.24 \text{ ft}^2}{20.6 \text{ ft}^2} = 2.5 \text{ ft}$$



CAD drawing 11. Elevator

11. Design of the Landing Gear and Weight and Balance

11.1 Landing Gear Design

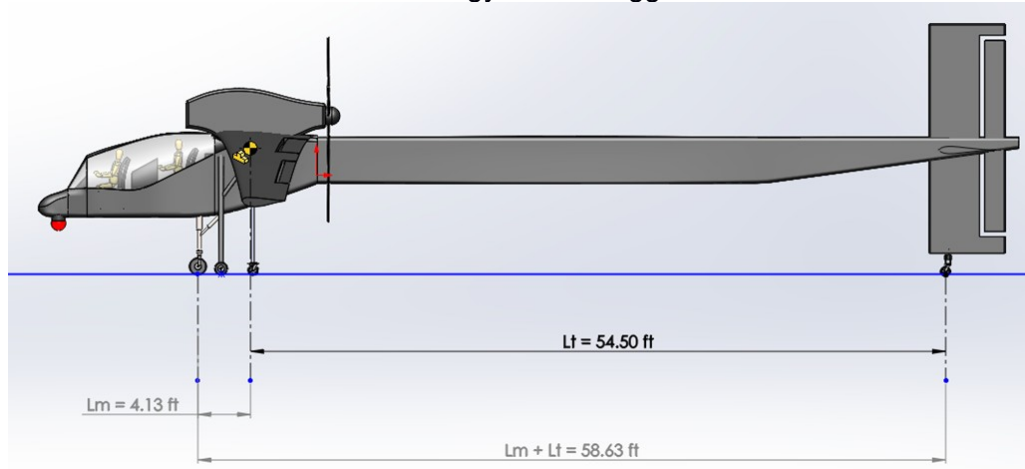
Due to the challenges associated with the design of an airplane capable of operating under unusual and difficult conditions, it may be convenient to adopt design measures that are not conventional. One of those challenges, for instance, involves the design and operation of the landing gear. Lift generation, especially during the take-off and land stages, is only possible if drag and weight are minimized.

Choosing a conventional retractable landing gear can help decrease drag, but the weight associated with gear extension and retraction mechanisms such as hydraulic systems add significant amount of weight.

The landing gear proposed here would need to be retractable yet lightweight. One such unconventional gear arrangement that could fit the operational characteristics of the Mars airplane is that incorporated by the Solar Impulse.

This landing gear employs a bicycle configuration with additional lateral supports that help increase lateral ground stability and sustain the structural integrity of the long wings.

Calculation of the static load per strut of the airplane will be approximated using the methodology for taildraggers:



CAD drawing 12. Calculation of tire size

$$P_t = \frac{W_i l_m}{l_m + l_t} \quad \dot{i} \quad \frac{W_i * 4.13 \text{ ft}}{58.63 \text{ ft}} = 91.6 \text{ Lbs} \quad \rightarrow \quad \frac{P_t}{W_i} = 0.07$$

$$P_m = \frac{W_i l_t}{n_s (l_m + l_t)} \quad \dot{i} \quad \frac{W_i * 54.5 \text{ ft}}{58.63 n_s} = 0.93 \frac{W_i}{n_s} \rightarrow \frac{2P_m}{W_i} = 0.93 \quad \text{with}$$

$n_s = \text{number of struts}$;

It follows that for these values the following data is obtained:

tail tire: $d_t \times b_t = 9 \text{€} \times 3.5 \text{€}$, *tire pressure = 55 psi*

main gear tire: $d_t \times b_t = 22 \text{€} \times 8 \text{€}$, *tire pressure = 35 psi*

Tip-over criterion

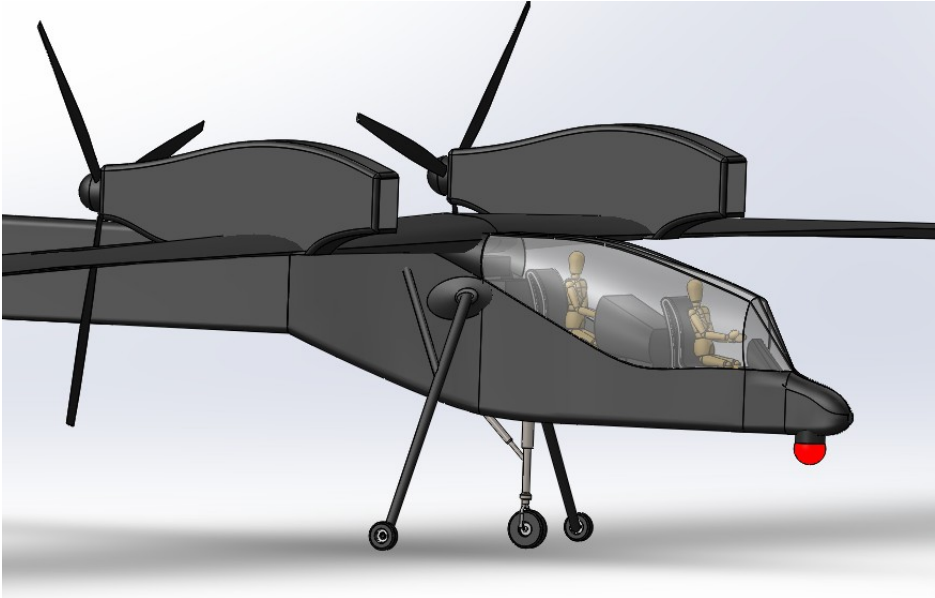
Analyses for the longitudinal and lateral tip-over criterion of the airplane are omitted since they are not necessary for this landing gear configuration.

Propeller ground clearance

Because the airplane doesn't rotate in either the take-off or landing stages due to the special configuration, propeller clearance is not critical. Nevertheless, the vertical

distance between the propeller tips and the ground, as seen below, provides an optimal clearance against debris.

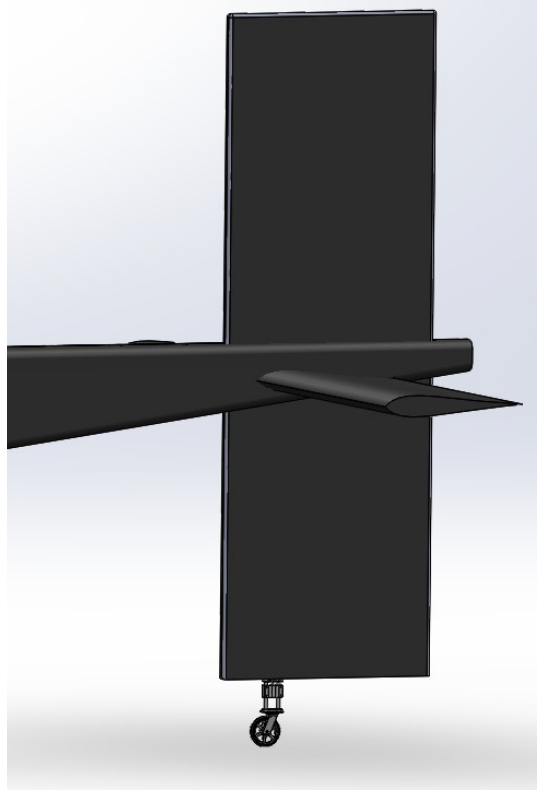
3-D views of the landing gear arrangement



CAD drawing 13. Detail of the landing gear arrangement



CAD drawing 14. Landing gear arrangement



CAD drawing 15. Detail of landing gear



CAD drawing 16. Landing gear arrangement

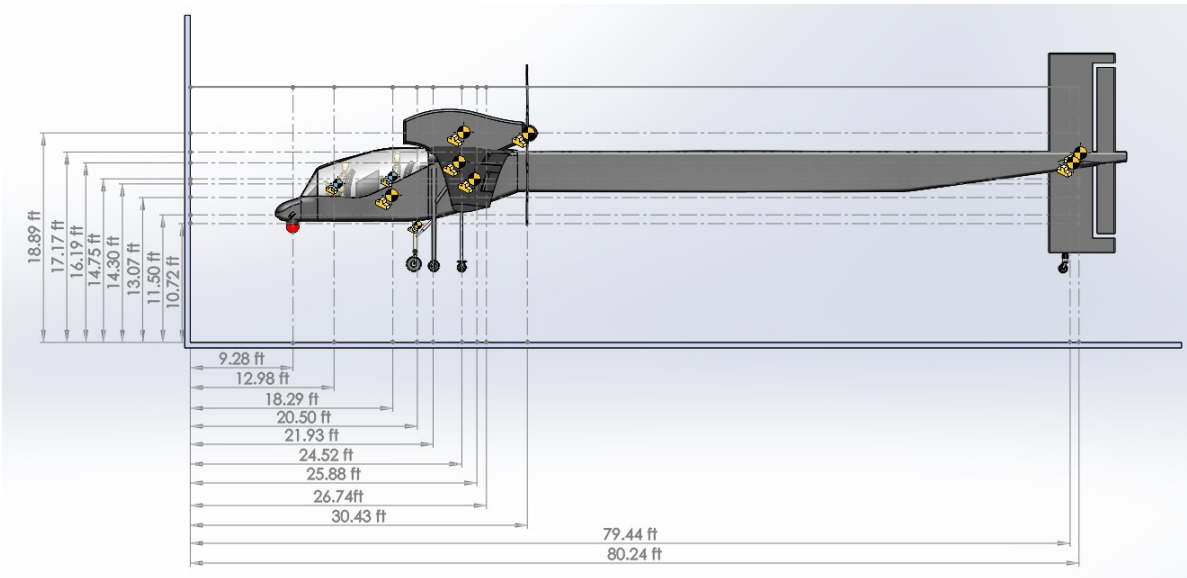


CAD drawing 17. Front view of the landing gear arrangement



CAD drawing 18. Side view of the landing gear arrangement

11.2 Weight and Balance

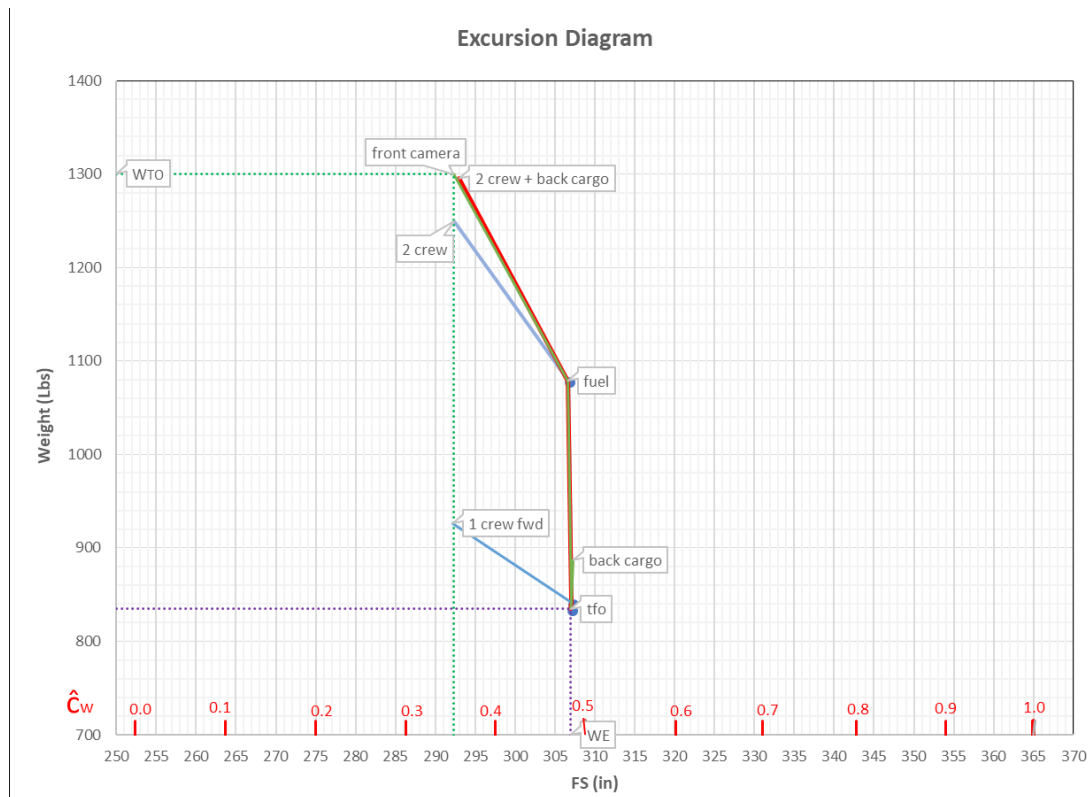


CAD drawing 19. Location of different components

Component	Weight (Lb)	x (in)	Wx (Lb-in)	z (in)	Wz (Lb-in)
Wing	167.51	297.6	49850.35	194.40	32563.54
Horiz. Tail	15.91	953	15165.33	194.40	3093.54
Vert. Tail	10.61	963	10216.31	206.00	2185.42
Fuselage	115.86	219.5	25431.19	156.80	18166.79
Gear Nose	12.56	246	3090.521	128.60	1615.61
Gear Main	50.25	263.2	13226.42	171.60	8623.31
Nacelles	44.67	294.2	13141.55	226.80	10130.88
Engine	184.26	320.8	59110.19	226.80	41789.87
Propellers	122.84	365.2	44860.85	226.80	27859.91
Fixed Equ.	110.28	219.6	24216.62	156.80	17291.28
WE	834.75	309.45	258309.32	195.65	163320.14
tfo	6.50	320.9	2086.89	226.8	1474.94
fuel	237.69	297.6	70735.13	194.4	46206.01
pilot front	85.20	155.8	13274.16	171.6	14620.32
pilot back	85.20	219.5	18701.40	177	15080.40
cargo	46.01	310.6	14290.08	177	8143.42
camera	5.11	111.4	569.48	138	705.46
WTO	1300.46	290.64	377966.47	191.89	249550.69

Table 16. Weight and balance analysis

Location of the Center of Gravity for Possible Loading Scenarios



Graph 11. Excursion diagram.

The excursion diagram shows a cg travel of about 14 inches or $0.15 Fr \cdot \dot{c}_w$. This agrees with normal values for twin engine, propeller-driven airplanes, which commonly display cg ranges of $0.12-0.22 Fr \cdot \dot{c}_w$, or 9 – 15 inches.

A summary of the cg range for this airplane is included below:

most fwd cg	x
in	293
ft	24.41667
most aft cg	x
in	307
ft	25.58333

Table 17. Forward and aft cg locations

12. Stability and Control

12.1 Static Longitudinal Stability

Calculation of \dot{X}_{ac}

$$\dot{X}_{ac} = \frac{\dot{X}_{ac_{wf}} + CL_{ah} \left[1 - \frac{d\epsilon h}{d\alpha} \right] \left[\frac{S_h}{S} \right] \dot{X}_{ac_h}}{1 + CL_{ah} \left[1 - \frac{d\epsilon h}{d\alpha} \right] \left[\frac{S_h}{S} \right] \frac{CL_{\alpha wf}}{CL_{\alpha wf}}}$$

$$C_{L_{\alpha f}} = F C_{L_{\alpha c}}$$

where the wing-body interference factor F is obtained from [appendix](#)

$$C_{L_{\alpha c}} = \frac{2 \pi AR_w}{2 + \sqrt{\frac{AR_{eff}^2 \beta}{k^2} \left[1 + \frac{\tan^2(\Lambda_{c/2w})}{\beta} \right]} + 4} = 8.4 / rad$$

$$\beta = \sqrt{1 - M^2} = \sqrt{1 - 0.55^2} = 0.83$$

$$AR_w = 3$$

$$\Lambda_{c/2w} = 0^\circ$$

$$k = \frac{CL_{\alpha_{atM}}}{\frac{2\pi}{\beta}}$$

$$CL_{\alpha_{atM}} = \frac{CL_{\alpha_{atM}=0}}{\sqrt{1-M^2}} \text{ (for subsonic speeds)}$$

$$C_{L_{\alpha_{atM}}} = \frac{2\pi AR_w}{2 + \sqrt{AR_w^2 \beta^2 \left[1 + \frac{\tan^2(\Lambda_{t/c})}{\beta^2} \right]} + 4} \text{ /rad}$$

$$C_{L_{\alpha_s}} = \frac{2\pi AR_h}{2 + \sqrt{\frac{AR_{eff}^2 \beta}{k^2} \left[1 + \frac{\tan^2(\Lambda_{c/2h})}{\beta} \right]} + 4}$$

For the horizontal stabilizer:

$$AR_h = 5$$

$$\beta = \sqrt{1-M^2} = \sqrt{1-0.55^2} = 0.83$$

$$\Lambda_{c/2h} = 0$$

$$k = \frac{CL_{\alpha_{atM}}}{\frac{2\pi}{\beta}} = 0.013$$

$$CL_{\alpha_{atM}} = \frac{CL_{\alpha_{atM}=0}}{\sqrt{1-M^2}} = 5.66/\text{rad} \quad (\text{for subsonic speeds})$$

$$C_{L_{\alpha_{atM=0}}} = \frac{2\pi AR_w}{2 + \sqrt{AR_w^2 \beta^2 \left[1 + \frac{\tan^2(\Lambda_{t/c})}{\beta^2} \right]} + 4} = 4.73/\text{rad}$$

$$CL_{ah} = 5.55/\text{rad}$$

The downwash gradient at the horizontal tail can be approximated as:

$$\frac{d\varepsilon_h}{d\alpha} = 4.44 \left[\sqrt{k_A k_\lambda k_h \cos \Lambda_{\frac{c}{4}}} \right]^{1.19} \frac{CL_{\alpha_{atM}}}{CL_{\alpha_{atM}=0}}$$

$$k_A = \frac{1}{AR} - \frac{1}{1+AR^{1.7}} = 0.024874$$

$$k_\lambda = \frac{10-3\lambda}{7} = 1.2571$$

$$1 - \frac{h_h}{b} \sqrt{\frac{i}{2l_h}} = 1.3294, \text{ where the } h_h \wedge l_h \text{ parameters are obtained statistically}$$

$$k_h = \sqrt[3]{i}$$

$$\frac{d\varepsilon_h}{d\alpha} = 0.106$$

$$\dot{X}_{ac_{wf}} = \dot{X}_{ac_w} + \dot{X}_{ac_f} \quad \text{where} \quad \dot{X}_{ac_w} = 0.25 \quad ,$$

$$\dot{X}_{ac_{wf}} = 0.2336$$

$$\dot{X}_{ac} = \frac{\dot{X}_{ac_{wf}} + CL_{\alpha h} \frac{\left[1 - \frac{d\epsilon h}{d\alpha}\right] \left[\frac{S_h}{S}\right] \dot{X}_{ac_h}}{CL_{\alpha wf}}}{1 + CL_{\alpha h} \frac{\left[1 - \frac{d\epsilon h}{d\alpha}\right] \left[\frac{S_h}{S}\right]}{CL_{\alpha wf}}} = \frac{0.2336 + 0.097 \frac{\left[1 - 0.106\right] \left[\frac{S_h}{1,445}\right] 8.5}{0.15}}{1 + 0.097 \frac{\left[1 - 0.106\right] \left[\frac{S_h}{1,445}\right]}{0.15}}$$

$$\dot{X}_{ac} = \frac{0.2336 + 0.00334 S_h}{1 + 3.93 * 10^{-4} S_h}$$

To obtain the \dot{X}_{ac} leg of the analysis, the weight per pound of the horizontal stabilizer is estimated as:

$$S_H = 101.2 \text{ ft}^2$$

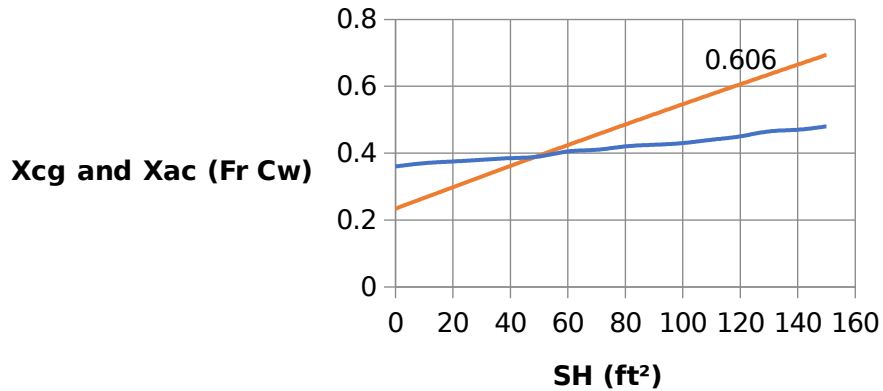
Using the previously estimated weight of the horizontal stabilizer (15.91 Lbs), the weight per pound is calculated as 0.157 Lbs.

Using the excursion diagram to visualize the aft cg shift as the weight of the stabilizer is increased from a value of 0 Lbs, the following relations could be obtained:

Sh (ft ²)	$\bar{X}_{cg}(Fr\bar{c}w)$	$\bar{X}_{ac}(Fr\bar{c}w)$	SM (%)
0	0.36	0.234	0.126
10	0.37	0.266	0.104
20	0.375	0.298	0.077
30	0.38	0.330	0.050
40	0.385	0.362	0.023
50	0.39	0.393	-0.003
60	0.405	0.424	-0.019
70	0.41	0.455	-0.045
80	0.42	0.486	-0.066
90	0.425	0.516	-0.091
100	0.43	0.546	-0.116
110	0.44	0.576	-0.136
120	0.45	0.606	-0.156
130	0.465	0.635	-0.170
140	0.47	0.665	-0.195
150	0.48	0.694	-0.214

Table 18. Calculation of horizontal tail are based on 10% SM

Static Longitudinal Stability



Graph 12. Static longitudinal stability

These calculations show that for a 10% margin of static stability, the horizontal tail must have a surface area of $S_H = 100 f t^2$. This indicates that the previous sizing of

$$S_H = 101.2 f t^2 \text{ was optimal.}$$

12.2 Directional Stability

Yawing-moment-due-to-sideslip derivative $C_{n\beta}$ (weathercock stability parameter)

$$C_{n_\beta} = C_{n_{\beta_w}} + C_{n_{\beta_m}} + C_{n_{\beta_v}}$$

$C_{n_{\beta_w}} \approx 0$, since wing contribution important only at high angles of attack .¹¹

$$C_{n_{\beta_m}} = -0.96 K_B \frac{S_s}{S} \frac{L_{fus}}{b} \sqrt{\frac{h_1}{h_2}} \sqrt[3]{\frac{w_2}{w_1}}, \text{ fuselage contribution}$$

$\dot{\alpha} \text{ rad}^{18}$

where K_B can be determined from the following equation:

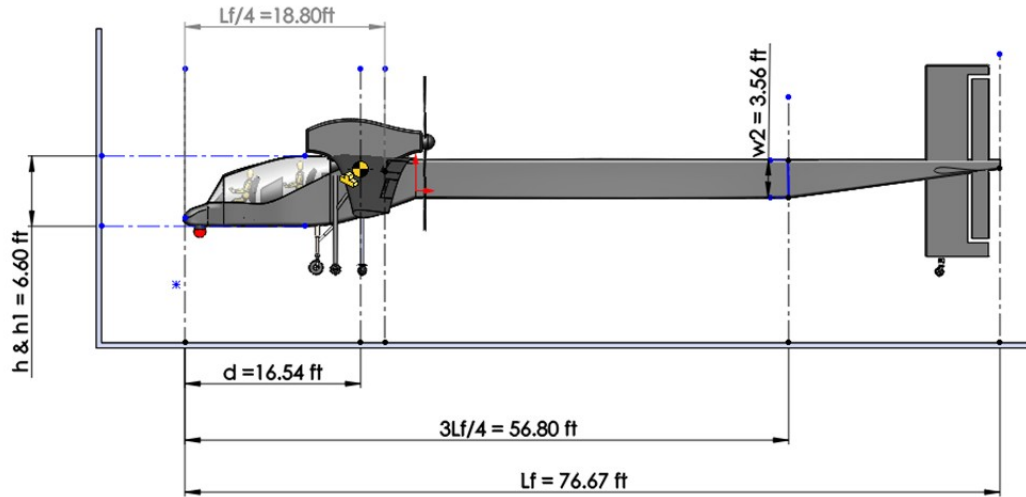
$$K_B = (K'_B - 0.0285) + 0.2857 \frac{d}{L_{fus}}$$

$\frac{l_f}{h}$	k'_B
2.5	0.175
3.0	0.150
4.0	0.125
5.0	0.080
6.0	0.055
7.0	0.038
8.0	0.025
10.0	0.005

Table 19. estimates for K'_B based on fuselage dimensions

$$\frac{l_f}{h} = \frac{76.67}{6.6} = 11.6 \rightarrow K'_B \approx 0.005$$

$$K_B = (K'_B - 0.0285) + 0.2857 \frac{d}{L_{fus}} = 0.038$$



CAD drawing 20. Parameters for the calculation of directional stability

$$C_{n_{\beta_{rot}}} = -0.00151 / rad$$

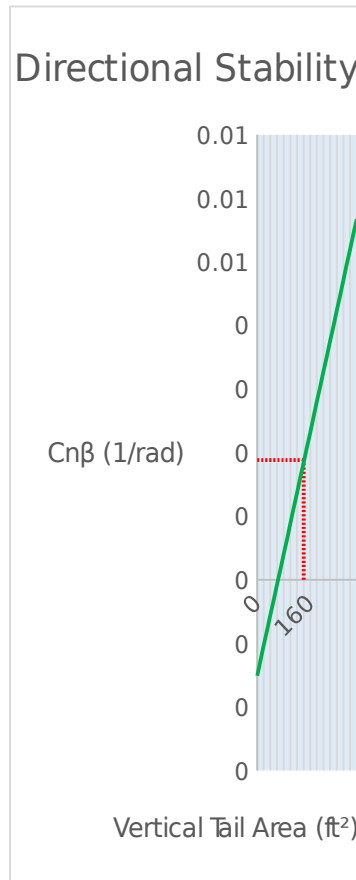
$$C_{n_{\beta}} = C_{L_{\alpha}} \eta_v \frac{S_v x_v}{S b} \left(1 - \frac{\partial \sigma}{\partial \beta} \right)$$

$$C_{L_{\alpha}} = \frac{2\pi AR_v}{2 + \sqrt{\frac{AR_{eff}^2 (1-M^2)}{k^2} \left[1 + \frac{\tan^2(\Lambda_{c/2})}{(1-M^2)} \right] + 4}} = 0.0951 / rad$$

$$AR_{eff} = 1.55 \frac{b_v^2}{S_v} = 4.65$$

$$\eta_v \left(1 - \frac{\partial \sigma}{\partial \beta} \right) = i \quad 0.724 + 3.06 \frac{\frac{S_v}{S}}{1 + \cos\left(\frac{\Lambda_c}{4}\right)} + 0.4 \frac{z_w}{h} + 0.009 AR_w = 1.435$$

$$C_{n_{\beta}} = 0 - 0.00151 (0.0695 \times 1.435) \frac{170.8 S_v}{1,445 \times 231} = 0.00188$$



Graph 13. Directional stability and vertical tail area

These findings show that for optimal directional stability, the area of the vertical stabilizer must be reduced by 17%. (from 170 ft² to 140 ft²).

14. Conclusions

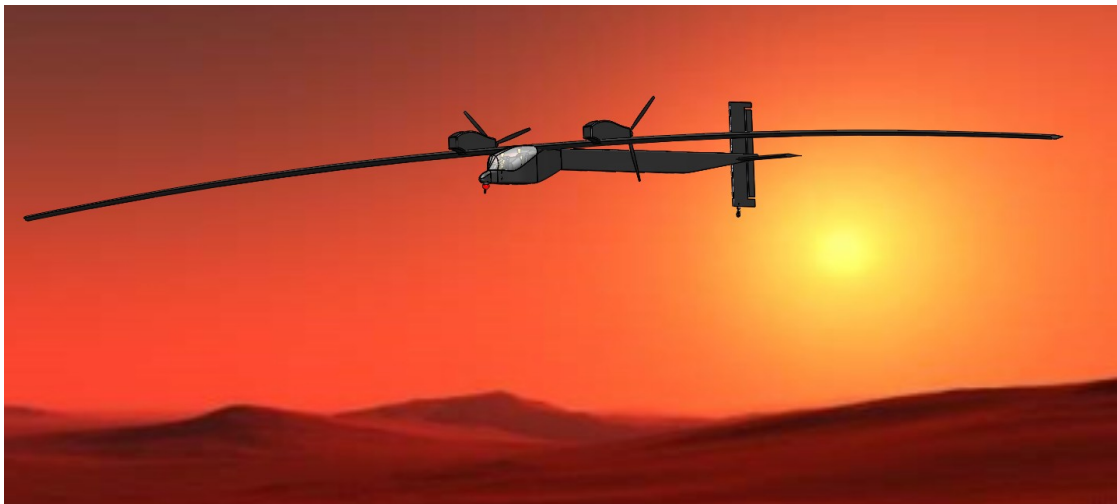
The data collected in this report confirms the difficulty associated with the design of an airplane capable of flying in the Martian atmosphere. Different variables and methods, part of the design followed in this report, often required drastic and unconventional measures. As expected, the weight of the airplane is a major

constraint as evidenced by the very wing loading obtained, $\left(\frac{W}{S} \right)_{i_c} = 0.9 \frac{Lb}{ft^2}$.

This leads to a design with a required high wing surface area $(S_w = 1,445 ft^2)$.

In addition, a very high wing aspect ratio $A=37$ was used in order to maximize L/D.

The selected airfoil, the NACA 4415, performed better than the other two options considered. As evidenced by the numerical simulation provided, the NACA 4415 generated substantial higher $C_{L_{max}}$ than the Apex-16 and LNV-109a at all tested conditions. Especial emphasis was made for the prediction of this airfoil at $\alpha=0^\circ$ due to projected take-off and landing configurations of the airplane. Several possibilities for the selection and integration of the propulsion system of the airplane were considered. Based on the pros and cons of each of these candidates, it was determined that an especially designed 4-cycle internal combustion engine performed better at the tested conditions. A bipropellant combination of UDMH and N_2O_4 was chosen due to their application at the given low temperature, where they remained in the liquid phase. The theoretical high-altitude propeller selected adapts better to the expected low Reynolds number. This 16-ft diameter, three bladed propellers determined from data extrapolation could theoretically provide an efficiency factor of 0.83 at cruise flight conditions. The landing gear configuration selection was dependent on the overall structural limitations of the airplane. Because large surface areas for the horizontal and vertical stabilizers were required, and due to low empennage weight constrains, it was convenient to adopt this unconventional bicycle configuration. The sizing of the horizontal and vertical stabilizers was backed by requirements of good directional and longitudinal static stability.



References

- [1] Kieffer, H. H. (1995). *Mars*. Tucson, AZ: Univ. of Arizona Press.
- [2] Mini-Sniffer Remotely Piloted Research Vehicle [Digital Image]. (2017, August 3). Retrieved January 27, 2018, from <https://www.nasa.gov/centers/armstrong/multimedia/imagegallery/Mini-Sniffer/index.html>
- [3] Leavin' on a Martian Jet Plane [Digital image]. (n.d.). Retrieved January 27, 2018, from https://hips.hearstapps.com/pop.h-cdn.co/assets/cm/15/05/54cb64f38ba3b_-_interplanetary-flight-sim-01-0313-de.jpg
- [4] Gonzalez, A. (2007, August 27). Computer-aided-design (CAD) image of the Matador Mars airplane concept [Digital image]. Retrieved January 27, 2018, from https://www.nasa.gov/centers/ames/images/content/183951main_med_Pizarro%20-%20Matador%2003.jpg
- [5] Calaba, D. (2017, August 6). [Digital image]. Retrieved January 27, 2018, from https://www.nasa.gov/sites/default/files/thumbnails/image/mars_prandtl-m.jpg
- [6] Pathfinder in flight over Hawaii [Digital image]. (2014, February 28). Retrieved January 27, 2018, from https://www.nasa.gov/sites/default/files/images/326814main_EC97-44287-1_full.jpg
- [7] Pathfinder Plus in flight over Hawaii [Digital image]. (2014, February 28). Retrieved January 27, 2018, from https://www.nasa.gov/sites/default/files/images/330281main_ED02-0161-2_full.jpg
- [8] Colozza, A. J. (2003). *Comparison of Mars aircraft propulsion systems*. Cleveland, OH: National Aeronautics and Space Administration, Glenn Research Center.
- [9] Kuhl, C. A. (2009). *Design of a Mars airplane propulsion system for the Aerial Regional-Scale Environmental Survey (ARES) mission concept*. Hampton, VA: National Aeronautics and Space Administration, Langley Research Center.

- [10] Colozza, A. (1998, March). *High Altitude Propeller Design and Analysis Overview*[PDF]. Cleveland, Ohio: Federal Data Systems.
- [11] Roskam, J., Dr. (2005). *Aircraft Design Part I: Preliminary Sizing of Airplanes*. Lawrence, KS: DARcorporation.
- [12] Rutan Voyager. (2017, September 06). Retrieved January 27, 2018, from <https://airandspace.si.edu/collection-objects/rutan-voyager>
- [13] Grob Grabs Altitude Record. (1995, November). *Flying*, 122(11), 30.
- [14] Torenbeek, E. (2010). *Synthesis of subsonic airplane design: an introduction to the preliminary design of subsonic general aviation and transport aircraft, with emphasis on layout, aerodynamic design, propulsion and performance*. Dordrecht: Kluwer.
- [15] Kocivar, B. (1978, July). Superdrone: Pilotless Mite will Sniff Out Pollution. *Popular Mechanics*, 66-69.
- [16] Angels in Paradise: The Development of the U-2 at Area 51. (2012, December 13). Retrieved March 01, 2018, from https://www.youtube.com/watch?v=nQnBJrj_-l8&t=462s
- [17] *Pathfinder: Leading the Way in Solar Flight* [PDF]. (2002, October). Edwards, CA: NASA Dryden Flight Research Center.
- [18] Perkins, C. D., & Hage, R. E. (2006). *Airplane performance stability and control*. Hoboken, NJ: Wiley.
- [19] Nicolai, L. M. (1975). *Fundamentals of aircraft design*. Xenia, Ohio: Mets.
- [20] Boeing Condor [Digital image]. (n.d.). Retrieved April 22, 2018, from http://notreally.info/transport/drones/condor/img//condor_boeing_condor_02
- [21] History-making UAV Propellers: The Boeing Condor. (2016, January 20). Retrieved April 21, 2018, from <http://hartzellprop.com/making-uav-propeller-boeing-condor/>
- [22] Perseus B Remotely Piloted Aircraft [Digital image]. (2014, February 14). Retrieved April 21, 2018, from <https://www.nasa.gov/centers/armstrong/news/FactSheets/FS-059-DFRC.html>
- [23] Perseus B Parked on Ramp - Close-up of Controllable-Pitch Pusher Propeller [Digital image]. (1999, September). Retrieved April 21, 2018, from <https://www.dfrc.nasa.gov/Gallery/Photo/Perseus/HTML/EC99-45152-6.html>
- [24] Huge Five-Bladed MT Propellers Help Grob 2C Reach Record Altitude Of 66,000 ft. [Digital image]. (n.d.). Retrieved April 22, 2018, from <http://sustainableskies.org/april-festival-electric-flight/>

[25] EMRAX 268. (n.d.). Retrieved May 24, 2018, from <http://emrax.com/products/emrax-268/>

[26] Bents, D. J., & Maldonado, J. (1998, April). *Propulsion System for Very High Altitude Subsonic Unmanned Aircraft*[PDF]. Williamsburg: NASA.

[27] Bents, D. J., & Maldonado, J. (1998, April). *Propulsion System for Very High Altitude Subsonic Unmanned Aircraft*[PDF]. Williamsburg: NASA.

Appendix A

AIRPLANE CATEGORY	airframe	propulsion group	fixed equipment	empty weight
PASSENGER TRANSPORTS				
short-haul jets	32	8	14	53
turboprops	32	13	14	58
pistons	30	21	16	66
		8.		
long-haul jets	25	5	9	42
turboprops	27	12	12	51
pistons	26	18	11	54
FREIGHTERS				
short-haul turboprops	35	13	8	56
long-haul turboprops	27	10	7	44
EXECUTIVE JETS				
	28	8	16	51

Table 1. percentage MTOW weight fractions

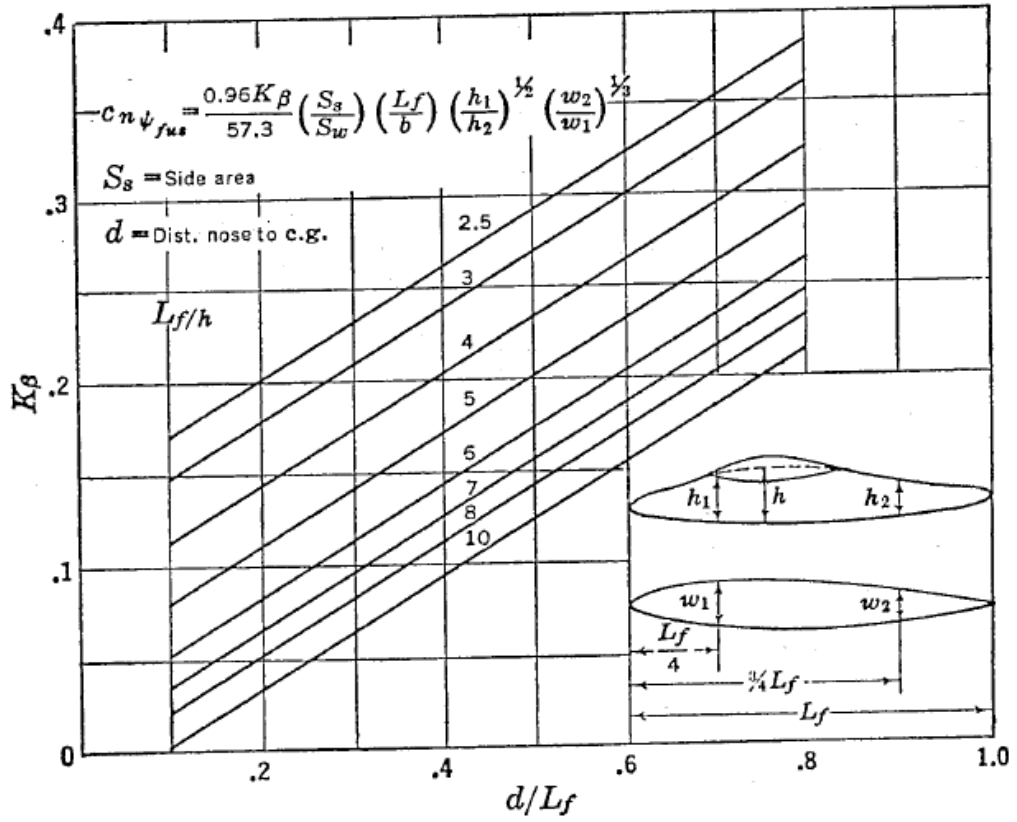


Table 2.

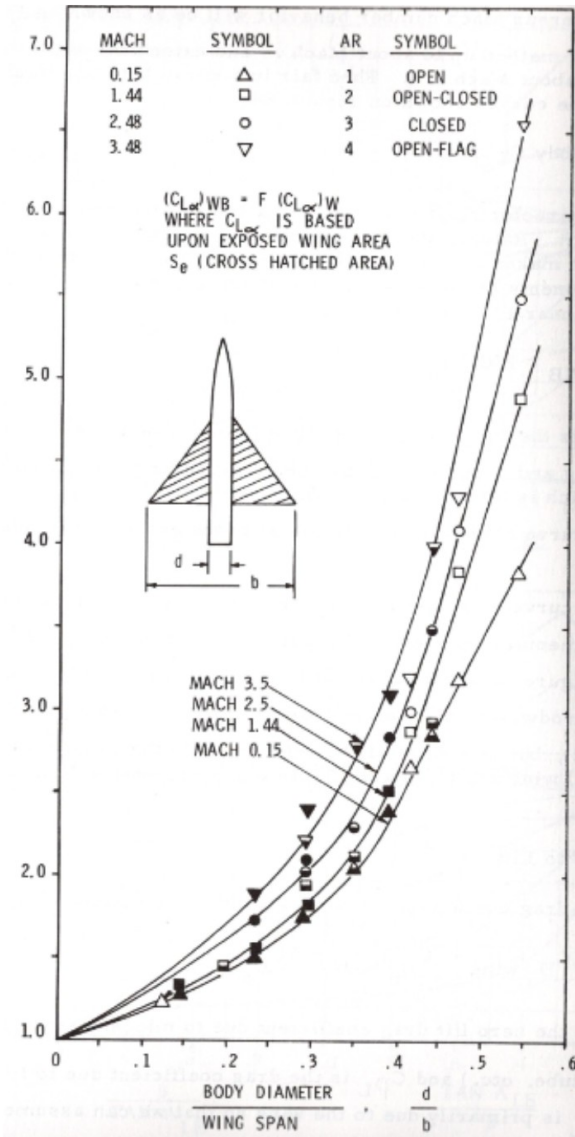


Fig. 11.3 Wing-Body Lift Interference Factor

Table 3.

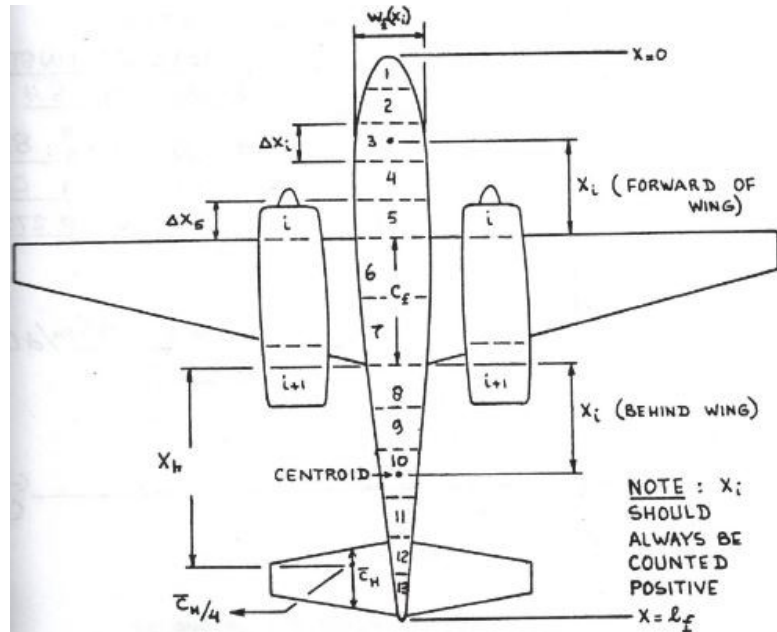


Figure 8.116 Layout for Computing Fuselage and (or) Nacelle Contribution to Airplane Aerodynamic Center Location

Table 4.

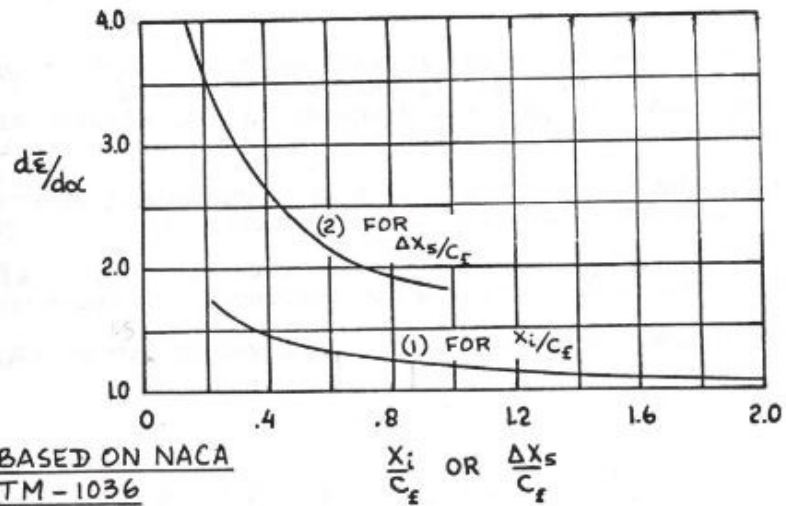


Figure 8.115 Effect of Fuselage (or Nacelle) Segment Location on Upwash Gradient

Table 5

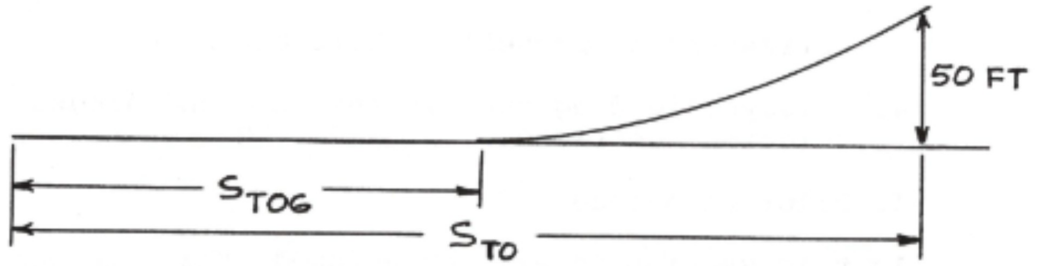


Table 6

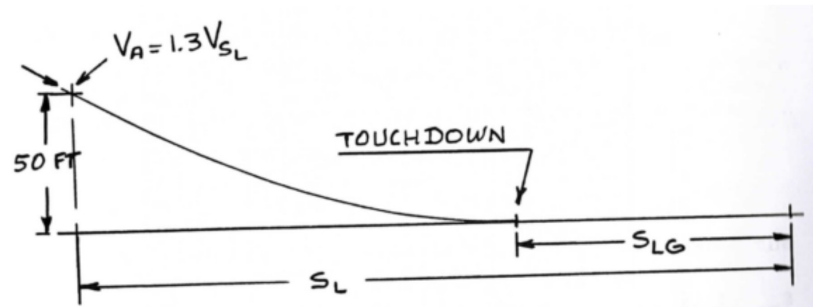


Figure 3.12 Definition of FAR 23 Landing Distances

Table 7